esa

ECMWF

ESA Contract Report

EORFIScan contract ESA AO/1-11605/22/NL/SD

Contract Report to the European Space Agency

Assessing RFI flags at passive microwave bands with an NWP model

Authors: David I. Duncan and Niels Bormann
Technical officer: Yan Soldo
September 2024

Abstract

Radio frequency interference (RFI) is a critical issue for numerical weather prediction (NWP), as a significant fraction of overall forecast skill comes directly from assimilation of passive microwave radiances. Underpinning the assimilation of microwave radiances is an assumption that observed signals are natural in origin, rather than man-made. As the microwave spectrum becomes more crowded, particularly at lower frequencies exploited for telecommunications, there is an increased risk that previously pristine parts of spectrum used for Earth observation contain interference, and consequently that forecast skill could be affected.

This document evaluates flagging of RFI provided by Zenithal Blue Technologies (ZBT) and Research and Development in Aerospace (RDA) for passive microwave bands of consequence for data assimilation in NWP. Specifically, frequencies from 6.9 to 89 GHz are analysed from the satellite-borne radiometers AMSR2 and AMSU-A. The RFI flagging is assessed using simulated radiances from the ECMWF model background, comparing differences of observed and simulated brightness temperatures (i.e. O-Bs) to indicate whether flagged data appear contaminated by unnatural emission signals not simulated by the model, assumed to be RFI. In order to do this, analysis of simulated radiances needs to be restricted to scenes where the forward modelling is of a consistently high quality, screening out difficult surfaces such as sea-ice and mountainous regions. Two one-month periods in 2022 have been evaluated.

In line with previous studies, significant RFI is seen at the lower frequencies observed by AMSR2, namely at 6.925, 7.3, and 10.65 GHz. RFI is also observed at 18.7 GHz, primarily around the coast of the United States. These identified regions of RFI include both direct sources and signals reflected off the ocean surface. No areas of RFI have been identified and corroborated by departure-based analysis at 23.8 GHz or above for the periods studied, with no significant RFI seen in the AMSU-A radiances studied here. RFI detection is perhaps most difficult at 10.65 GHz over sea, with relatively weak but frequent RFI observed primarily in the seas around Europe as reflected signals from direct broadcast geostationary satellites. The issue of false positives (RFI flagged for a clean scene) is not a serious concern in this analysis, with at most 0.05 to 0.2% of the likely RFI-free observations being flagged as potentially contaminated. However, false positives due to geophysical signals are prevalent in some areas such as coastlines and sea-ice edges, and a known antenna pattern bias in AMSU-A radiances causes false positives in stratospheric channels. Further work is recommended for identifying low-level RFI over sea at C- and X-bands, as these are crucial channels for SST sensitivity and more affected by interference than currently assimilated frequencies. In particular, newly identified sources of 6.925 GHz RFI over sea will require mitigation for this channel's effective use in an assimilation system.

Plain Language Summary

Satellite measurements of the Earth depend on specific frequency bands of the electromagnetic spectrum, some of which are protected exclusively for Earth observation whilst others have shared use with other application areas. There is increasing pressure on parts of the microwave spectrum, primarily from telecommunications, and the concern is that some crucial bands for Earth observation will be impinged upon or rendered useless if these spectral bands are not vigilantly protected. For passive observations, this is because man-made sources of radiation—known as radio frequency interference or RFI—can partially or fully obscure the signals of interest from the Earth's surface and atmosphere. In the most dangerous cases for physical modelling, artificial sources can be mistaken as real geophysical signals if the interference is within the range of plausible natural variability. In this study, simulated observations from a numerical weather prediction (NWP) model are used to assess the identification of observations contaminated by RFI. We find that low frequency microwave channels (6-18 GHz) observe significant

RFI, predominantly near areas of high population density but with large regional variability. Signals of reflected RFI are most prevalent along the USA coastline, in the waters around Europe, and to a lesser extent in the western Pacific. The identified RFI corroborated by NWP analysis remains at frequencies of 18.7 GHz and below, with none yet seen at 23.8 GHz and above in the two months of data analysed from 2022.

1   Introduction

Radio Frequency Interference (RFI) is a general term to describe unwanted signals in the radio spectrum, which consists of radiation between 3 Hz and 3000 GHz (wavelengths from kilometres down to 0.1 mm). In the case of passive microwave remote sensing of the Earth, RFI is unnatural (i.e. man-made) signals of microwave radiation that interfere with measuring Earth's natural emission. Sources of RFI can be incredibly varied: e.g. telecommunications, household appliances, poorly shielded cables, direct broadcast satellites at adjacent bands, military radars. Concerns about interference in passive microwave bands used for observing the Earth have increased in recent years (Palmer *et al.*, 2021), as the demand for spectrum for telecommunications has steadily increased. Such concerns are most acute for frequencies at 20+ GHz, as higher frequency bandwidth has become increasingly attractive for telecommunications' 5G and soon 6G networks, whereas the meteorological community has been accustomed to these higher frequencies remaining more or less pristine for Earth observation.

Microwave radiometers for Earth observation use frequency bands that have specific measurement sensitivities, for example surface temperature or liquid cloud drops. Most of these bands exist in so-called "protected bands" for Earth observation as specified by the International Telecommunications Union (ITU), an entity that oversees the use of spectrum internationally under the auspices of the United Nations. The use of radio spectrum is heavily regulated both internationally and nationally, balancing the needs of diverse users and stakeholders. Internationally, the ITU sets policy and these policies are discussed and revised roughly every 3-4 years at the World Radiocommunication Conference (WRC). Enforcement of the ITU standards is typically done at the national level, such as when a specific source is found operating in a protected band. Groups such as the Space Frequency Coordination Group (SFCG) coordinate reporting of identified RFI between space agencies[1]. Some frequency bands are specifically dedicated for Earth observation, defined as EESS (passive) allocations with either exclusive access or shared access with active services. A full list of regulations published by the ITU is available[2], with footnote 5.340 in volume 1 mentioning the EESS bands for which all emissions are prohibited (i.e. these are bands exclusively for Earth observation).

It is common for engineers and scientists to discuss microwave radiometry in terms of frequency bands with letter designations[3]. The band names typically used in meteorology are not entirely in the NATO or IEEE conventions, and instead waveguide names for frequency bands are used. Table 1 details the frequency bands included in this study, along with examples of satellite instruments that observe within these bands. In this report, the bands will be discussed primarily using the centre frequencies in gigahertz.

This study will not describe any potential RFI sources as "illegal" even if they appear to occur in a protected band. One of the reasons is that it is not always known whether the entire Spectral response function (SRF) of a given channel is indeed fully within the protected band. For instance, although the specification document says that a sensor has an 18.7 GHz centre frequency and 200 MHz bandwidth,

---

[1]See https://www.sfcgonline.org/ for references and identified cases of RFI at various bands

[2]The most recent year available is currently 2020: https://www.itu.int/pub/R-REG-RR-2020

[3]Supposedly, the names for these bands were purposefully difficult to remember so as to protect wartime intelligence

Table 1: Band names, central frequencies, and a selection of satellite sensors (present and future) from which these bands are measured. Exclusive EESS passive frequency bands are given in italics, whereas bands shared with active services are marked by an asterisk (*). Some frequencies such as C-band are used for Earth observation and noted by ITU but for shared use with other applications.

Band Name	Frequency [GHz]	Instrument and Centre Frequency
C	6.425 - 7.25	AMSR2: 6.925, 7.3 CIMR: 6.875
X	10.6 - 10.68 * *10.68 - 10.7*	AMSR2, GMI, MWRI, CIMR: 10.65
Ku	18.6 - 18.8 *	AMSR2, GMI, MWRI, MWI, AMR-C, etc.: 18.7
K	*23.6 - 24.0*	AMSR2, GMI, MWRI, AMSU-A, ATMS, etc.: 23.8
Ka	*31.3 - 31.8*	AMSU-A, ATMS, MWI, MWS: 31.4
Ka	36.0 - 37.0 *	AMSR2, GMI, MWRI, CIMR: 36.5 SSMIS: 37.0
V	*50.2 - 50.4*	AMSU-A, ATMS, SSMIS, MWI, MWS: 50.3
V	52.6 – 59.3	AMSU-A, ATMS, MWS: 52.8, 53.6, 54.4, 54.9, 55.0
W	*86.0 - 92.0*	ATMS: 88.2 AMSU-A, AMSR2, GMI, etc.: 89.0 SSMIS: 91.65

its true SRF may have some sensitivity outside this bandwidth and thus it could pick up some signals outside of the protected band. The responsibility for errant signals can thus lie with both emitters and receivers. There has been a push for space agencies to make SRFs public for operational microwave sensors (English *et al.*, 2020), and this has improved significantly in recent years, but the majority of heritage sensors like those analysed in this study do not have SRFs published.

As a general rule, the lower microwave frequencies used for Earth observation have been more susceptible to RFI contamination, as lower frequencies are more commonly used for telecommunications due to their lower attenuation in the atmosphere. In contrast, frequencies from about 22 GHz and up are less desirable for telecommunications due to water vapour and hydrometeor attenuation that largely increases with frequency. The lowest commonly used microwave frequency for passive Earth observation is L-band, or around 1.4 GHz, with the SMOS and SMAP missions still operating in 2024[4]. These missions have encountered widespread RFI from terrestrial sources, with identification and mitigation of RFI at L-band necessary to make these radiances usable over several continents. At C-band (near 7 GHz), RFI was first found by the AMSR-E sensor on the Aqua satellite particularly over urban areas (Njoku *et al.*, 2005). At the X- and Ku-bands, roughly 10 and 18 GHz here[5], RFI has been identified from terrestrial and satellite-borne sources (Wentz, 2015; Draper, 2017); these include sources identified over land as well as reflected signals over sea and scattering surfaces such as snow and ice (McKague *et al.*, 2010). At this time, there are only rare and sporadic RFI signals in the literature at 23 GHz and

---

[4]The P-band BIOMASS mission will operate at an even lower frequency (435 MHz) with a radar, and there are also space weather missions that observe at low frequencies.

[5]Typically Ku-band is 12-18 GHz, but to better distinguish between the 18 and 23 GHz bands, which could both be said to lie within the K-band, here the 18.7 GHz band is referred to as Ku-band.

higher frequencies. However, the radio environment is constantly evolving, and as new allocations are given to commercial operators near dedicated Earth observing bands, there is increasing concern about RFI in these higher frequency bands. Specifically, changes to ITU regulations following WRC19 led to a change of rules near the crucial 23.8 GHz band used by numerous operational satellites for column water vapour, with a lower level of protection from emissions in adjacent bands than recommended by several studies. It may be too early to see the impact of this change in this study, however, as it can take years for manufacturers to create devices that exploit newly opened spectrum.

2 Results in the Literature

In this section, we review some key findings from papers in the literature, focusing on the results rather than the methods of RFI detection in these papers. This is not an exhaustive review of the literature, as there have been dozens of RFI-focused papers on microwave radiometry in the past twenty years or so.

Earlier papers on RFI for microwave imagers largely focused on AMSR-E, as this was the first space-borne radiometer with C-band channels (Li *et al.*, 2004; Njoku *et al.*, 2005) and these experienced obvious RFI contamination over urban areas. Interference at X-band was also noted in AMSR-E observations, which saw prevalent 10 GHz signals over England, Italy, and Japan; the TMI instrument on board the TRMM satellite was the first space-borne imager with a 10 GHz channel (launched in 1997), but due to its inclined orbit over the tropics only, it had not observed these locations.

Reflected signals near 18 GHz have been found in several studies using data from TMI, GMI, AMSR-E, SSMI, and WindSat (e.g. McKague *et al.*, 2010; Adams *et al.*, 2010), with signals predominantly around the coastal United States. Others have found reflected signals at 10 GHz, mainly affecting seas around Europe. In both cases these are mainly from direct broadcast television satellites in geostationary orbit (Zou *et al.*, 2014; Zabolotskikh *et al.*, 2015), and their signals are thus relatively predictable functions of viewing geometry (Scanlon *et al.*, 2024), though of course subject to abrupt changes when these satellites are retired or new ones begin operation. Some reflected signals have been found in C-band at 7.3 GHz with AMSR2 around Europe and East Asia (Wu *et al.*, 2020).

The AMSR2 instrument and its successor AMSR3 both have channel suites influenced by the likelihood of RFI at lower frequencies. After the experience of AMSR-E, with large and widespread RFI signals at C-band, the AMSR2 design featured a second C-band frequency at 7.3 GHz, intended to permit better detection of anomalous signals in C-band. However, they found that there is arguably more interference at 7.3 GHz than at 6.925 GHz (Draper, 2018, their Fig. 7), albeit quite dependent upon the region examined. For example, Zabolotskikh *et al.* (2015) noted examples of RFI in AMSR2 radiances in the two C-band channels using spectral difference methods, and Wu *et al.* (2019) demonstrates how spatial patterns of RFI at the two C-band channels can be quite different. The future AMSR3 instrument will feature an extra X-band channel centred at 10.25 GHz with a much wider bandwidth (500 vs. 100 MHz) to better identify RFI at X-band. In this context, it is notable that RFI has been found in the WindSat 10.7 GHz band by several studies, as WindSat used a larger bandwidth (300 MHz) and was thus venturing outside protected bands, thereby being more susceptible to RFI. However, Draper and Stocker (2017) point out that staying within protected bands has limited usefulness in real terms—improved noise performance is possible with wider bands, whereas this WindSat channel suffered from significant RFI only near Europe. This is a good example of the difficult trade-offs that are faced by space agencies when planning future missions that observe at lower microwave frequencies.

For microwave frequencies used in NWP systems, the most comprehensive study of RFI to date is Draper (2018). This paper examined the GMI, TMI, AMSR2, and WindSat radiometers at channels ranging

from 6.925 GHz on AMSR2 up to 19.35 GHz on TMI. That paper built upon earlier work on the GMI radiometer specifically (Draper, 2015; Draper and Newell, 2015), given GMI's significance as a reference radiometer for calibrating the GPM constellation. In those papers, in addition to Wentz and Draper (2016) and Wentz (2015), the significance of RFI in the cold-sky mirror is also noted as an issue that can affect microwave imagers; these effects are usually clear in a time series of cold-view counts and thus generally removed at source as part of the level 1 data processing. Draper (2018) catalogued the regions with most significant RFI, and crucially noted the time-varying aspect of sources. For instance, RFI at 10.65 GHz V-pol was rarely seen over Turkey in the early 2000s, but by the 2010s it was quite common. There are also examples of RFI mitigation at the national level being effective, such as over Japan at 6.925 GHz, where about half the country was covered by RFI in the early 2000s but it became less common and less severe over the following 15 years.

For frequencies near the water vapour absorption feature at 22.235 GHz and above, instances of RFI have been rare or nonexistent in the literature. There has been evidence of contamination in the 21.3 GHz channel of TMI (Le Vine, 2019), but none yet at the more commonly used 23.8 GHz band that the authors are aware of. There have also been cases of strong RFI in the Ka-band from upward pointing radars (Group, 2022). However, such cases have thankfully been sporadic and rare in the literature when compared to interference at lower frequencies.

In terms of locations where a given frequency typically experiences RFI, the following broad conclusions can be drawn from the above-mentioned studies, with the caveat that they are based on time periods from several years ago and the RF environment is constantly evolving:

- **6.925 GHz** signals mainly near major metropolitan areas, particularly in North America, Brazil, India, and the Middle East

- **7.3 GHz** signals mostly over land and large cities, but with key hotspots in Ukraine and Belarus, Indonesia and Southeast Asia, Spain, Morocco, Turkey, and Central America; some reflected signals near Europe and East Asia

- **10.65 GHz** interference is mainly around Europe, with isolated sources also seen in places like China, Japan, Egypt; reflected signals common in the Mediterranean and waters off Western Europe

- **18.7 GHz** interference is almost entirely reflected signals around the United States (typically over sea but also off the Great Lakes and snow-covered areas in that region), though some localised sources over land do exist

- RFI signals above 19.3 GHz have been rare and generally not impacted use of these bands in retrievals or data assimilation

A key aspect to note about RFI studies in the literature is the detection limit and how this relates to observation errors in data assimilation. Some studies do not state a specific detection limit, as this will depend upon elements such as surface type, polarisation, and the sensitivity to clouds and precipitation of that frequency band. The Draper (2018) method sets thresholds explicitly, with for example 15K and 20K set for 10.65 GHz over ocean and land, respectively, representing conservative limits for detection that aim to minimise false alarms. More stringent thresholds can be used for temporally-averaged radiances, as low as 5K for 10 GHz over land (Draper, 2015). The Wu et al. (2019) and Wu et al. (2020) papers use a baseline detection limit of 5K over land and ocean.

It is worth emphasising that for data assimilation, the most dangerous RFI has roughly the same magnitude as the assigned observation errors. Thus RFI at imager channels that is maybe 2-5K can be quite problematic, as these could be assigned significant weight in the assimilation, whereas RFI of say 30K will either be rejected or heavily down-weighted by standard quality control procedures. This becomes even more acute for V-band sounding channels, as weak RFI of say 1K could be virtually impossible to identify by most methods but could be assigned significant weight in the assimilation due to these channels' small observation errors. The C- and X-band channels over sea that exhibit reflected RFI are quite problematic in this regard, as the assigned observation errors are on order 1K and could lead to artificially warmer SSTs in the model if the weaker RFI-affected radiances were assimilated in a coupled atmosphere-ocean assimilation system.

3   Data and Methods

The period for this study is two months in 2022, March and October. Unless otherwise stated, the analysis will focus on March 2022. This is simply to focus the analysis. Most signals analysed were consistent in both months.

3.1   Satellite Instruments

In this study we focus on passive microwave radiometers that observe at commonly used frequencies for Earth observation. These instruments were chosen because their frequency bands are of interest for Earth system modelling both now and in the future—assessing the RFI environment now is a crucial aspect of planning for future satellite missions. These instruments and the platforms they fly on are briefly described below. Table 2 contains channel numbers and centre frequencies for the instruments.

The Advanced Microwave Scanning Radiometer-2 (AMSR2) is a one-off instrument that is the sole payload on the Global Change Observation Mission-Water (GCOM-W) satellite operated by JAXA. GCOM-W was launched in 2012 and flies in a sun-synchronous, low-Earth orbit in the A-Train constellation with a 13:30 ECT in its ascending node. AMSR2 is a follow-on instrument from AMSR-E, which launched in 2002, and a predecessor of the AMSR3 instrument that is expected to launch later in 2024. The AMSR series of instruments have pioneered C-band observation in particular, allowing new applications of microwave radiometry such as soil moisture retrieval that require low frequency measurements[6]. Its low frequency channels have made AMSR2 part of the backbone of global SST and sea-ice concentration measurements. AMSR2 is a conically-scanning radiometer, measuring at 7 frequency bands in both vertical and horizontal (hereafter V and H) polarisation, with a roughly 55 ° constant incidence angle. The geolocations of each AMSR2 frequency are effectively co-located on the ground (Maeda *et al.*, 2016). One of the key reasons that AMSR2 observes at two frequencies within C-band (6.925 and 7.3 GHz) is that AMSR-E experienced consistent RFI at the 6.925 GHz band, and thus the addition of a nearby band centred at 7.3 GHz was intended to aid in detection of RFI signals (Okuyama and Imaoka, 2015). AMSR2 footprint sizes range from 35x62 km at 6.925 GHz to 3x5 km at 89 GHz. The upcoming ESA mission Copernicus Imaging Microwave Radiometer (CIMR) will observe at four of the frequency bands used by AMSR2, and RFI mitigation will be a key aspect of the CIMR mission.

The Advanced Microwave Sounding Unit-A (AMSU-A) instrument is a cross-track scanning radiometer that measures primarily at V-band frequencies to provide atmospheric temperature profile information

---

[6]WindSat launched in 2003 and had 6.8 GHz channels, but these data were not as freely available.

Table 2: Channel numbers and central frequencies (in GHz) given with polarisation for AMSR2 and AMSU-A. Polarisations for AMSU-A are "quasi" vertical and horizontal (QV, QH), as the polarisation changes with scan position (un-polarised at nadir). The AMSR2 89 GHz channels are actually two separate scans to provide full spatial coverage, the A- and B-scans, but treated as single channels here (as they are in the JAXA BUFR file).

Ch.#	AMSR2	AMSU-A
1	6.925V	23.8V
2	6.925H	31.4V
3	7.3V	50.3V
4	7.3H	52.8V
5	10.65V	53.596H
6	10.65H	54.4H
7	18.7V	54.94H
8	18.7H	55.5H
9	23.8V	$57.29\text{H} = f_0$
10	23.8H	$f_0 \pm 0.217$
11	36.5V	$f_0 \pm 0.3222 \pm 0.048$
12	36.5H	$f_0 \pm 0.3222 \pm 0.022$
13	89.0V	$f_0 \pm 0.3222 \pm 0.010$
14	89.0H	$f_0 \pm 0.3222 \pm 0.0045$
15	-	89.0V

from oxygen absorption bands. AMSU-A has been part of the payload on nine different satellite platforms since 1998, with five still active in 2024. Assimilation of AMSU-A radiances has been a key driver of forecast improvements in NWP due to their consistency, quality, and longevity. In addition to its V-band channels between 52-58 GHz for atmospheric temperature sounding, AMSU-A holds window channels centred at 23.8, 31.4, 50.3, and 89.0 GHz. The 23 and 31 GHz channels will be assimilated at ECMWF starting in 2024, following Duncan *et al.* (2022a). All of the AMSU-A frequencies are also flown on follow-up instruments such as the ATMS from NOAA and the future MWS from EUMET-SAT. In this study, AMSU-A data are taken from the EUMETSAT satellite Metop-C, the final and most recently launched AMSU-A instrument.

Conically-scanning radiometers such as AMSR2 have a near-constant view angle, leading to an Earth incidence angle of about 55 °. Cross-track radiometers such as AMSU-A have a variable view angle that depends upon the scan position. This means that the zenith angle for AMSU-A ranges between 0 and 48.95 degrees. The sounding channels thus have greater sensitivity to the surface and see further down into the atmosphere at near-nadir scan positions, whereas outer scan positions with large zenith angles have less surface sensitivity. Considering potential RFI, it is crucial to note that AMSU-A has FOVs that grow larger as a function of zenith angle; for example, AMSU-A has a 48x48 km FOV at nadir but a 149x79 km FOV at its outer-most scan position (Robel and Graumann, 2014). A point source of RFI could thus appear weaker if it is observed near the scan edge, because it would be averaged together with a larger area of natural radiation; furthermore, nadir observations have less atmospheric attenuation due to a shorter path length, whereas observations near the scan edge have less surface sensitivity. Conical scanners like AMSR2 have consistent FOV sizes across the scan.
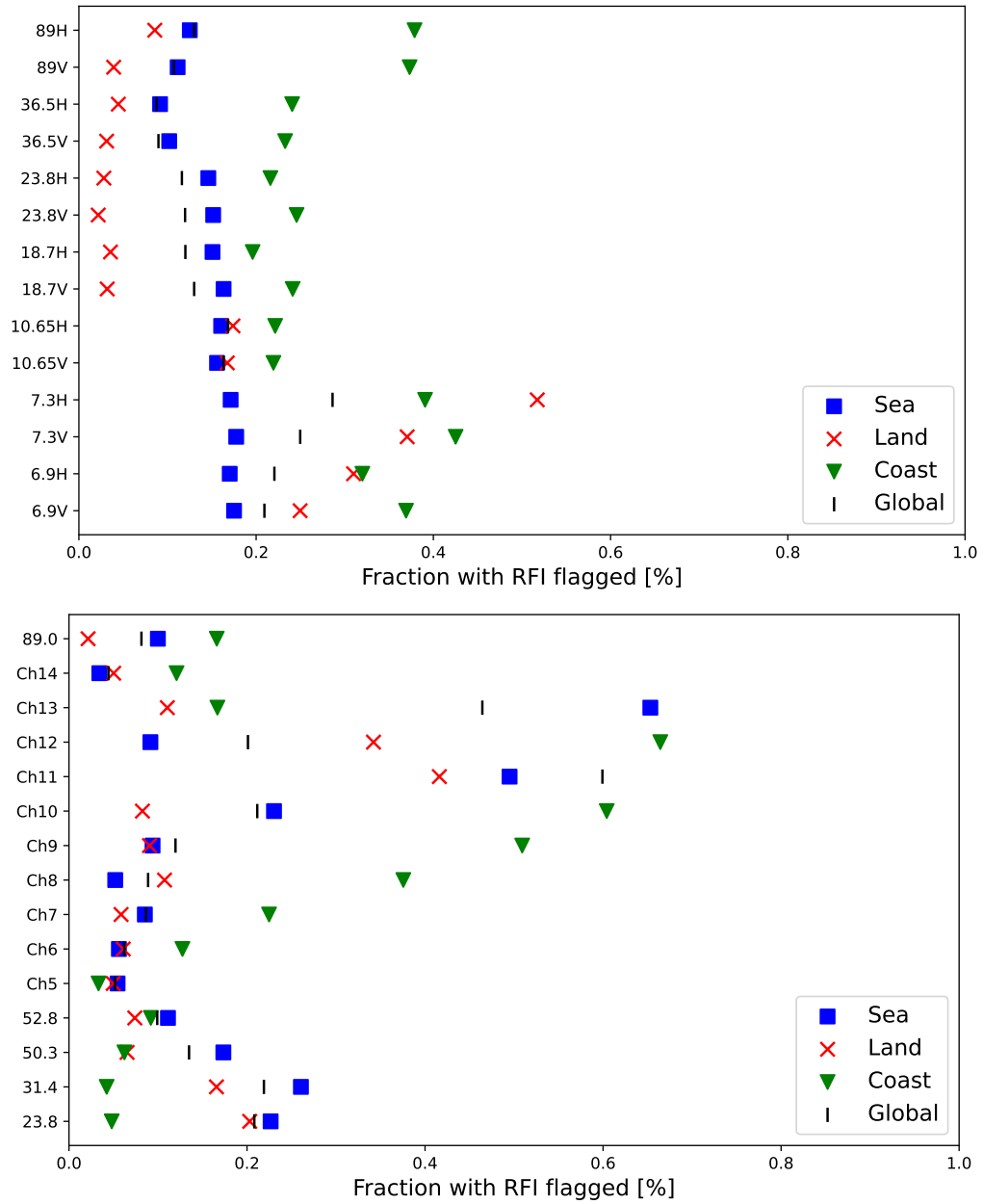
Figure 1: Percentage of total radiances flagged as RFI, radiances marked as either medium or high confidence. AMSR2 (top) and AMSU-A on Metop-C (bottom) for March 2022, comprising roughly 3e8 and 9e6 total points, respectively. Coast is defined as 1 to 95% land fraction.

3.2 RFI Detection

The RFI detection software was implemented in a cloud computing framework, a collaboration between ZBT and RDA. ZBT provides the main scientific expertise in RFI detection, building upon a substantial body of work at L-band for the SMOS mission (e.g. Oliva *et al.*, 2016, 2021; Weston *et al.*, 2021). The RFI detection algorithm, the Earth Observation RFI Scan software (EORFIScan), which builds upon the Ground RFI Detection System (GRDS), consists of several methods that will be described in a companion report from ZBT. In this project, the RFI confidence levels were limited to four categories:

- None: No flag is set (no RFI suspected)

- Low: Low RFI threshold; low confidence of RFI and more false positives

- Medium: Medium confidence of RFI

- High: High RFI threshold; high confidence of RFI and fewer false positives

These flag levels are separated by the confidence of EORFIScan in the presence of RFI, not necessarily the severity of interference. Internally for EORFIScan, there are actually 5 different tests run, which were then distilled into the 3 possible RFI flags used in this project due to the availability of bits in the input BUFR files. The above flags are individual but can also be added together, i.e. Medium+High will contain all points where either of the flags is set. In most of the results presented we will focus on data flagged as either medium or high confidence RFI, but some analysis of the different flag levels is provided later in Sec. 5.3.

The global frequency of radiances flagged by EORFIScan over the month of March 2022 is given in Fig. 1. Data are given as a global total, and also broken up into ocean, coast, and land categories, counting data flagged as either medium- or high-confidence. Land-based RFI is considered the dominant concern for C-band channels, whereas near-zero fractions of mid-frequency channel radiances are flagged as RFI over land. Curiously, mid-stratosphere channels on AMSU-A have relatively high fractions of observations flagged; these are likely an artefact, as the spatial structures of flagged points could map onto temperature structures in the stratosphere. Similarly, the lower frequency channels on AMSU-A have more observations flagged over sea than over land, but these appear linked to sea-ice features.

Figures 2 and 3 show the spatial distribution of flagged data for a selection of AMSR2 and AMSU-A channels. There are many features here that could be discussed, but we will largely leave this discussion for the results section, where regions of persistent RFI will be analysed. A few features will not be analysed later, however, and are worth mentioning here. For example, the lower AMSU-A frequencies exhibit numerous coastal areas that are flagged, and this pattern leads us to believe these are false positives, likely caused by a combination of the very large and variable footprint of AMSU-A and its cross-track scanning pattern. Some other geographic features are evident in the AMSU-A frequency maps such as the Himalayas and some weather signals like the SPCZ; likewise some of the noisier stratospheric channels (such as channel 13 in the figure) exhibit flagged points that do not appear related to any identifiable source. For AMSR2, there are some clear areas of false positives that are consistent across two or three frequencies, such as on the edge of Antarctic sea-ice.

Specific to AMSU-A (which has a cross-track scanning mechanism), a pattern was discovered in which EORFIScan is more likely to flag outer scan positions. This is seen in Fig. 4, with the medium- and high-confidence flag fractions shown as in the previous figure. The scan positions 3 and 28 stand out quite clearly, and this matches a position in the instrument with well-known biases due to antenna pattern corrections being insufficient. In fact, the outermost 3 scan positions on each side of AMSU-A are screened
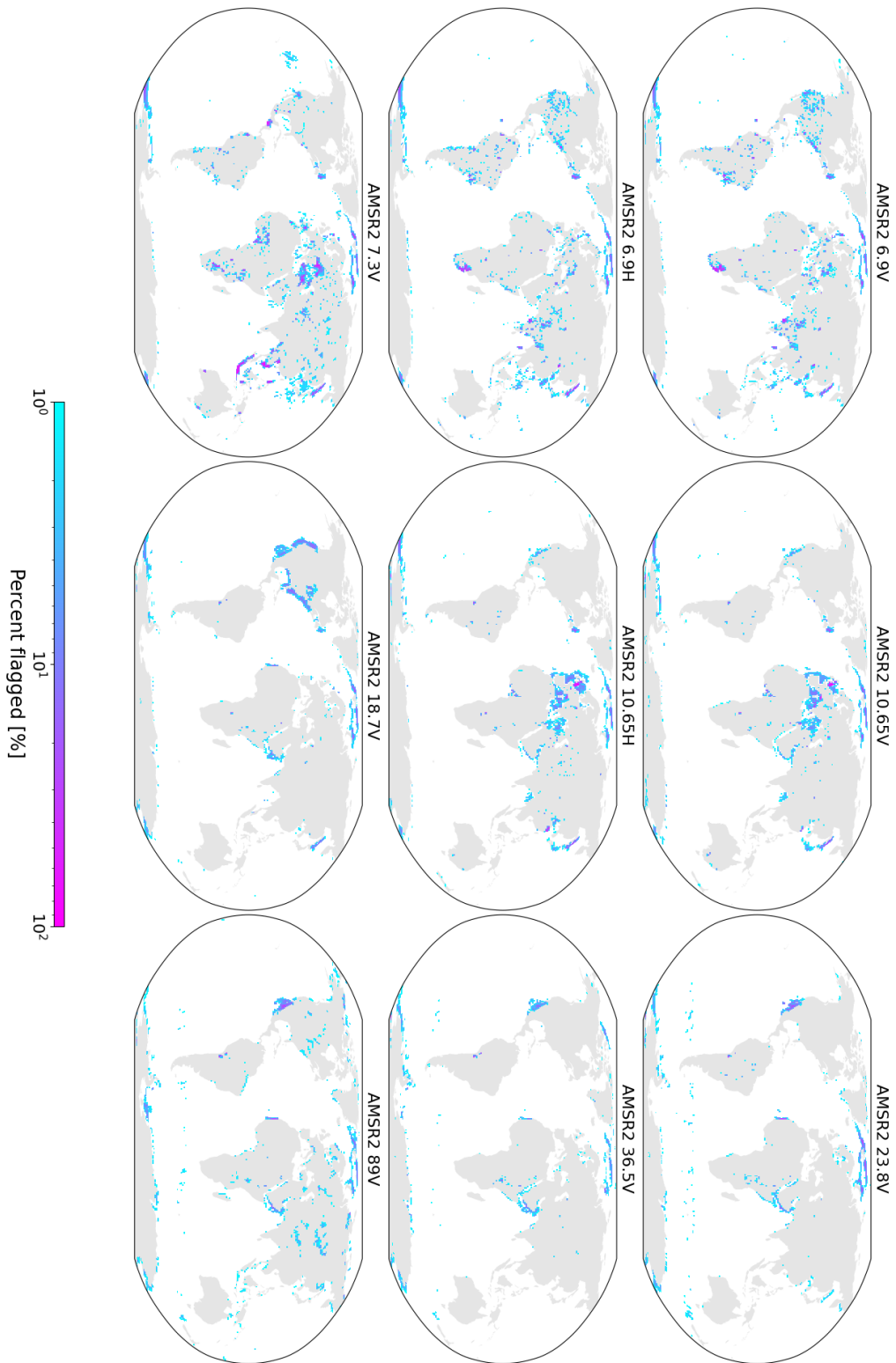
Figure 2: Frequency of AMSR2 observations flagged for RFI at medium and high confidence, March 2022. Data gridded at 1 degree.
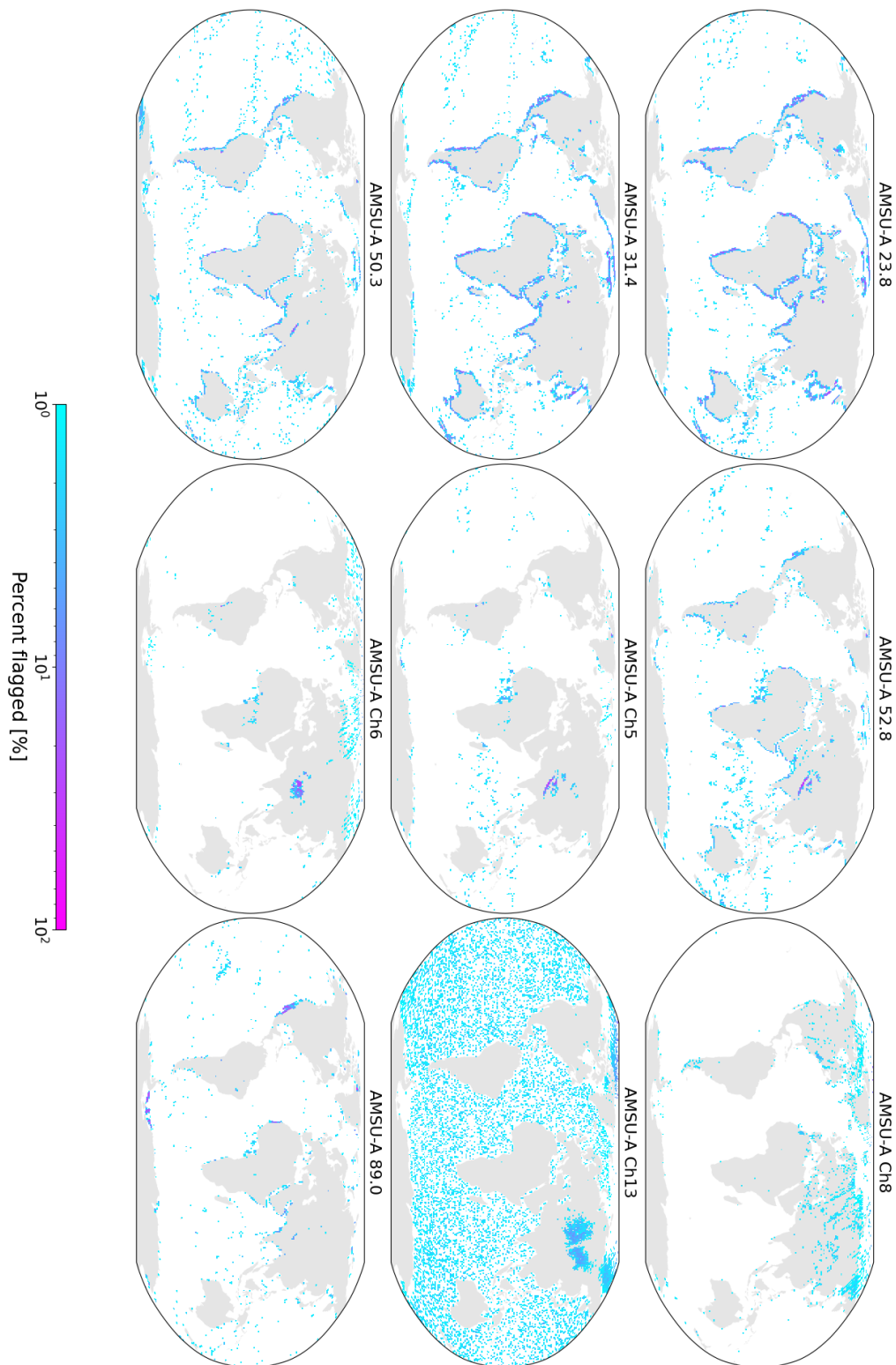
Figure 3: Frequency of AMSU-A observations flagged for RFI at medium and high confidence, March 2022. Data gridded at 1 degree.
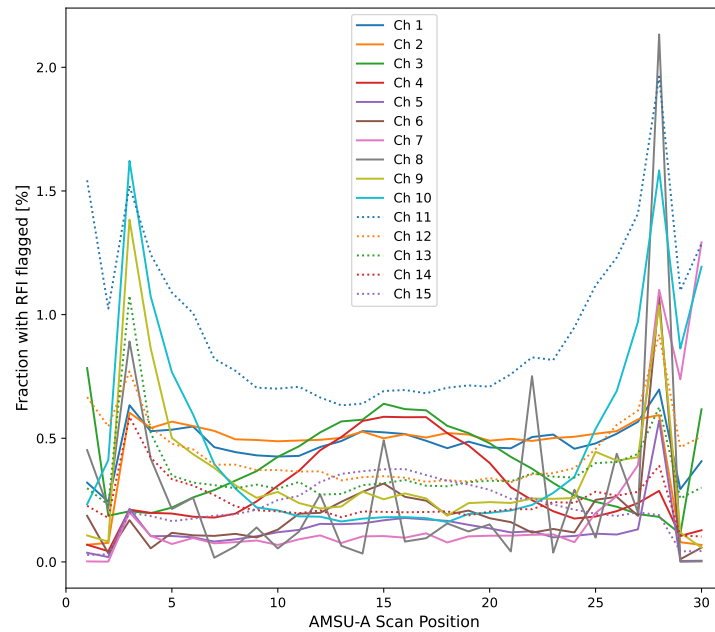
Figure 4: As Fig. 1 but as a function of scan position for AMSU-A, considering all global data.

out at ECMWF prior to assimilation, due to these strong bias features (Duncan *et al.*, 2022b). This appears to indicate that EORFIScan picks up this bias feature as potential RFI, especially for higher-peaking channels for which this is a defining feature of the total variability. There is also a scan-dependent feature visible for the channels with mixed surface and sounding sensitivity such as channels 3-6; especially for channels 3 and 4, the scan positions most likely to observe any RFI are near nadir, where they have the greatest visibility of the surface. This feature is in line with expectations, as greater sensitivity to the surface should mean a greater likelihood of experiencing interference.

Lastly, as Draper (2018) is a key reference as discussed in Sec. 2, we can produce a map with different channels together to allow comparison to their Figure 2. To put all frequencies on one map, we use the same 1 degree grid as before and plot the highest frequency with flagged data points above a given threshold. Fig. 5 shows two different thresholds, 1 and 5%, just for the V-pol channels of AMSR2 and again using the medium- and high-confidence flagging from ZBT. The H-pol maps, as well as V-pol maps from October 2022, are found in the Appendix.

4   Departure Calculation, Characteristics, and Analysis

For the analysis of RFI detection, this project uses the background departures, or O-B (observation minus background), from the IFS at Cycle 49r1[7]. The reason to use the ECMWF model background, i.e. the short-range forecast in observation space, is that the model provides an accurate, 3D representation of the Earth system at any given time, providing a strong constraint for assessing abnormal radiative behaviour at microwave wavelengths.

Crucially, the IFS simulates natural emission signals only, so the model background provides an estimate

---

[7]Official documentation is not yet available for Cycle 49r1, but most of the documentation for the previous model cycle is applicable (ECMWF, 2023). Cycle 49r1 will become the operational ECMWF model version in autumn 2024.
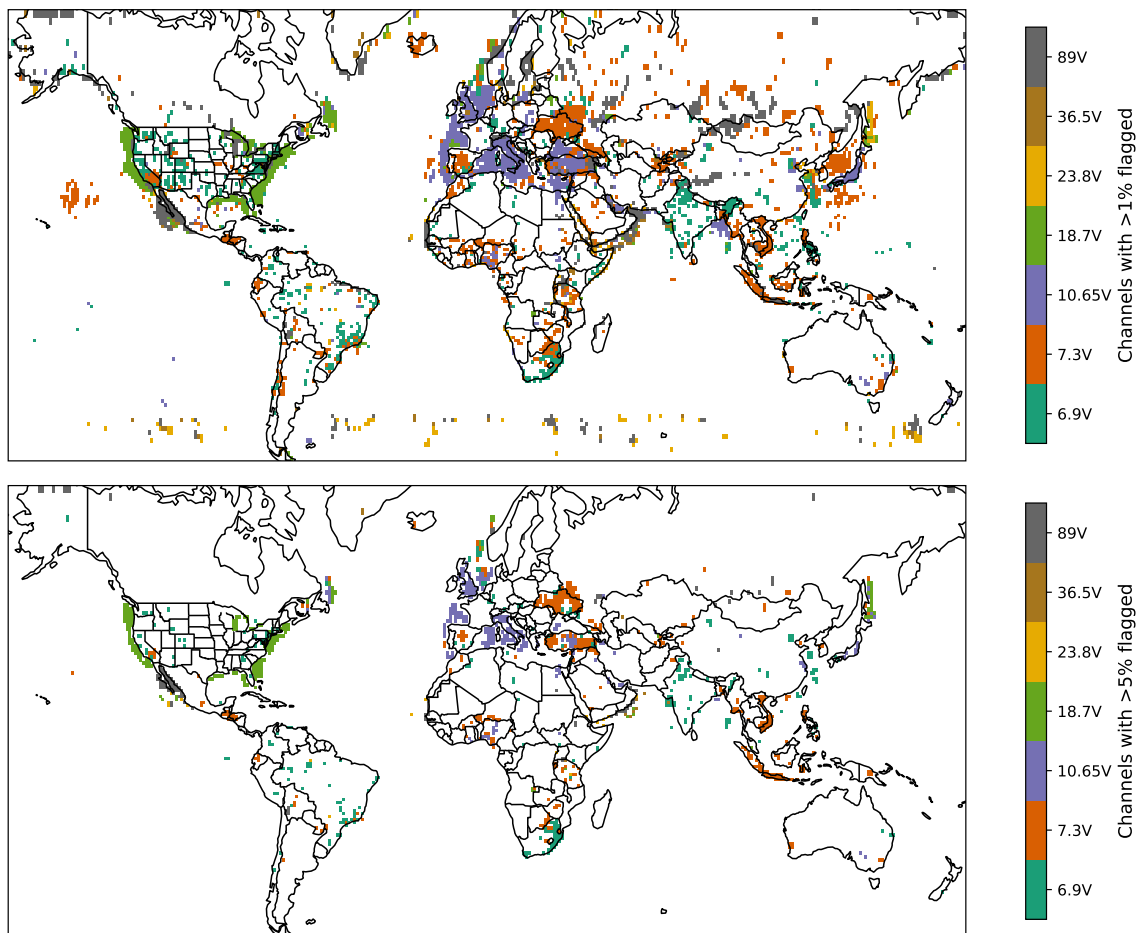
Figure 5: Prevalence of flagged data points at each AMSR2 frequency over March 2022, in the style of Draper (2018, their Fig. 2). The threshold used for plotting is 1% on the top panel, 5% for the bottom panel. Only V-pol channels are shown, with H-pol maps given in the Appendix 22.

of the total distribution of radiances that are expected in the absence of any RFI. These natural signals include only sources from the Earth's surface, atmospheric gases, and the scattering and emission from hydrometeors. No solar term is currently included, though atmospheric down-welling radiation reflected off the surface is included.

This section describes the input data, how background departures are calculated, and how the departures are analysed in this project.

4.1 Level 1 Radiances

This project is based upon the level 1 radiance data provided for NWP use in the BUFR format by space agencies (typically called L1B). These files provide latitude, longitude, and Brightness temperature (TB) given in Kelvin, among other fields. If RFI flags are provided in the BUFR file by the space agency, these are disregarded in this study—only the RFI flags created by ZBT are analysed.

For the assimilation of radiances at ECMWF, there is a variational bias correction applied to ensure that the radiances have a mean centred around zero. This correction is calculated as part of the 4D-Var

minimisation and is known as VarBC (Dee, 2004). In this project, the un-corrected radiances were used by ZBT to calculate the RFI flags. As described below, the background departures do include a bias correction term.

Ordinarily for microwave assimilation in the IFS, level 1 radiances are either superobbed (i.e. averaged together) or thinned to a specified spacing as part of the observation pre-processing. This is done to mitigate representation errors and spatial error correlations in addition to decreasing data volumes. However, in this project the radiances are passed through the IFS with no superobbing or thinning applied[8]. This means that the total data volumes of observational data are significantly larger than normal, permitting finer spatial patterns to be observed. Furthermore, basic screening for unphysical TBs is applied for microwave radiances in the IFS pre-processing; this has been removed for this project, for example allowing an observed TB of 380K to pass into the IFS that would normally be rejected by a simple TB bounds check. Thus all level 1 radiances are passed through the IFS for the instruments analysed in this study, with no thinning, averaging, or pre-selection.

4.2   Calculation of Background Departures

The model background includes atmospheric gases such as oxygen and water vapour that attenuate passive microwave radiation, in addition to representing clouds and precipitation that can emit and scatter microwaves. The IFS also provides surface temperatures, concentrations of sea-ice, snow cover, and so on over the entire globe, providing a constraint for expected radiative behaviour in all conditions. These fields are coupled with geolocation and viewing geometry information from the level 1 radiances to simulate the observed TBs using RTTOV-SCATT, version 13 (Geer et al., 2021). Slant-path radiative transfer is used for sounders following Bormann (2017). Surface emissivity is provided over ocean by the SURFEM-Ocean model (Kilic et al., 2023). Over land, emissivities are retrieved using a designated window channel with good surface sensitivity (Karbou et al., 2006; Baordo and Geer, 2016). For AMSR2 this is the 18.7V channel, whereas it is 50.3V for AMSU-A. The retrieved emissivity is extrapolated to other frequencies for imagers such as AMSR2 using spectral signatures from an emissivity atlas (Geer et al., 2022), and assumed constant in frequency for AMSU-A.

Departures are defined as below, including a bias correction term to harmonise the IFS background with the observations (see Table 4 in Geer et al. (2022) for an example of the bias correction predictors used for AMSR2 channels). It should be noted that the choice to include the *BC* term in departure statistics has downsides, in that areas of strong model bias that may be mitigated by VarBC could potentially mask some small RFI signals. However, especially in the case of AMSR2 that has global 5K biases at some channels relative to the IFS (Duncan et al., 2024), it is preferable to use bias-corrected departure statistics as this is expected to aid in isolating the RFI signals of interest.

$$D_{BC} = (O - B) - BC \tag{1}$$

Background departures are computed for every channel and every geolocation. The experiments run for this project use 12hr long-window, delayed-cutoff assimilation cycles, so the maximum length of the short-range forecast is 12hr. Due to the delayed cutoff and the generally good reliability of the sensors used in this study, most 12hr assimilation windows are fully populated with data. The forecast model is run at TCo399 final model resolution in the experiments, or about 29 km horizontal spacing.

An example of observations, background equivalents, and departures is given in Fig. 6, showing AMSR2

---

[8]For a view of superobbed radiances, see Appendix Fig. 24

and AMSU-A observations over Europe at 10.65 and 31.4 GHz, respectively. Here the observed values shown (top row) are not bias-corrected, but the departures shown do incorporate bias correction. These panels highlight several important aspects of these observations. First, the high density of AMSR2 observations is evident, with 243 observations per scan compared to 30 for AMSU-A. Second, despite bias correction being applied, there are clear areas of model bias seen over various surfaces. For example at 10.65 GHz, we can clearly see where data are used for the sea-ice retrieval (Geer, 2024) up near Iceland, but the non-assimilated radiances over the rest of the global ocean exhibit a positive bias of about 4-5 K. This is a known bias relative to the reference sensor GMI (Berg *et al.*, 2016), and not fixed currently by VarBC due to the very low weight that VarBC weights receive in the 4D-Var minimisation for non-assimilated data. For AMSU-A 31.4 GHz, this is an assimilated channel over sea and the bias characteristics relative to the IFS largely look good, though coastlines are clear in several places with large departures, indicative of the lack of a footprint FOV operator for AMSU-A in the IFS (Geer *et al.*, 2022). Third, some surface types such as snow cover, sea-ice, and high orography are more challenging to model, as seen over areas such as Finland, the Bay of Bothnia, and the Alps.

To emphasise that even channels nearby in frequency space can exhibit distinct RFI sources, Fig. 7 shows the six lowest-frequency channels from AMSR2, with V-pol and H-pol departures side by side. Several features are notable, both in terms of potential RFI and clear forward model biases. The H-pol channels exhibit strong biases over certain regions due to poor emissivity retrieval estimates, e.g. western Norway, the Netherlands and Denmark, and in north Africa. The 6.925 and 7.3 GHz channels appear to see point sources of RFI in the North Sea between Scotland and Norway, though the different bands observe different point sources. This is a tell-tale sign of RFI, as nearby frequencies have nearly identical sensitivity to atmospheric and surface signals, whereas RFI is likely to reside in a narrow spectral range that is unlikely to be seen across multiple channels. Thus a feature of convective precipitation absent in the model should manifest as a positive departure at multiple frequency bands, but strong positive departures at 6.925 but not 7.3 GHz (or vice versa) are very likely RFI. The comparison of 6.925 and 7.3 GHz departures makes certain urban areas in Spain, Germany, and Italy stand out as likely RFI sources as well. There is probable reflected RFI at 10.65 GHz that is seen at H-pol but not V-pol off the coast of the Netherlands; the two polarisations agree more on the probable RFI in the Bay of Biscay. Some sources appear stronger at H-pol than V-pol, though there are also instances of clear RFI at V-pol but not H-pol at the same frequency, for example at 7.3V southeast of the Shetland Islands. These are just a few of the numerous features one can pick out from a subsection of two AMSR2 orbits, illustrating the manifold nature of this problem.

4.3 Departure-based Analysis

Although the model background is usually within a few Kelvin of the observed TB, there are regions and scenarios in which the model estimates are better than others. For example, scenes that are clear-sky in both the observation and the model are typically modelled within 2K for AMSR2 over ice-free oceans. Non-frozen land scenes are modelled with enough fidelity for some imager channels at 36 GHz and above to be assimilated in the IFS (Geer *et al.*, 2022), albeit with larger observation errors than over sea. In contrast, scenes with non-zero sea-ice concentrations can see 20K+ errors due to incorrect sea-ice fractions, poor emissivity modelling of the surface, or erroneous estimates of skin temperature from the model. Similarly, coastlines are challenging to model accurately.

Thus for analysis of RFI, it makes sense to limit the analysis to regions and scenes where the forward modelling of TBs from the IFS is sufficiently accurate. The following criteria are used for screening out observations from the departure analyses:
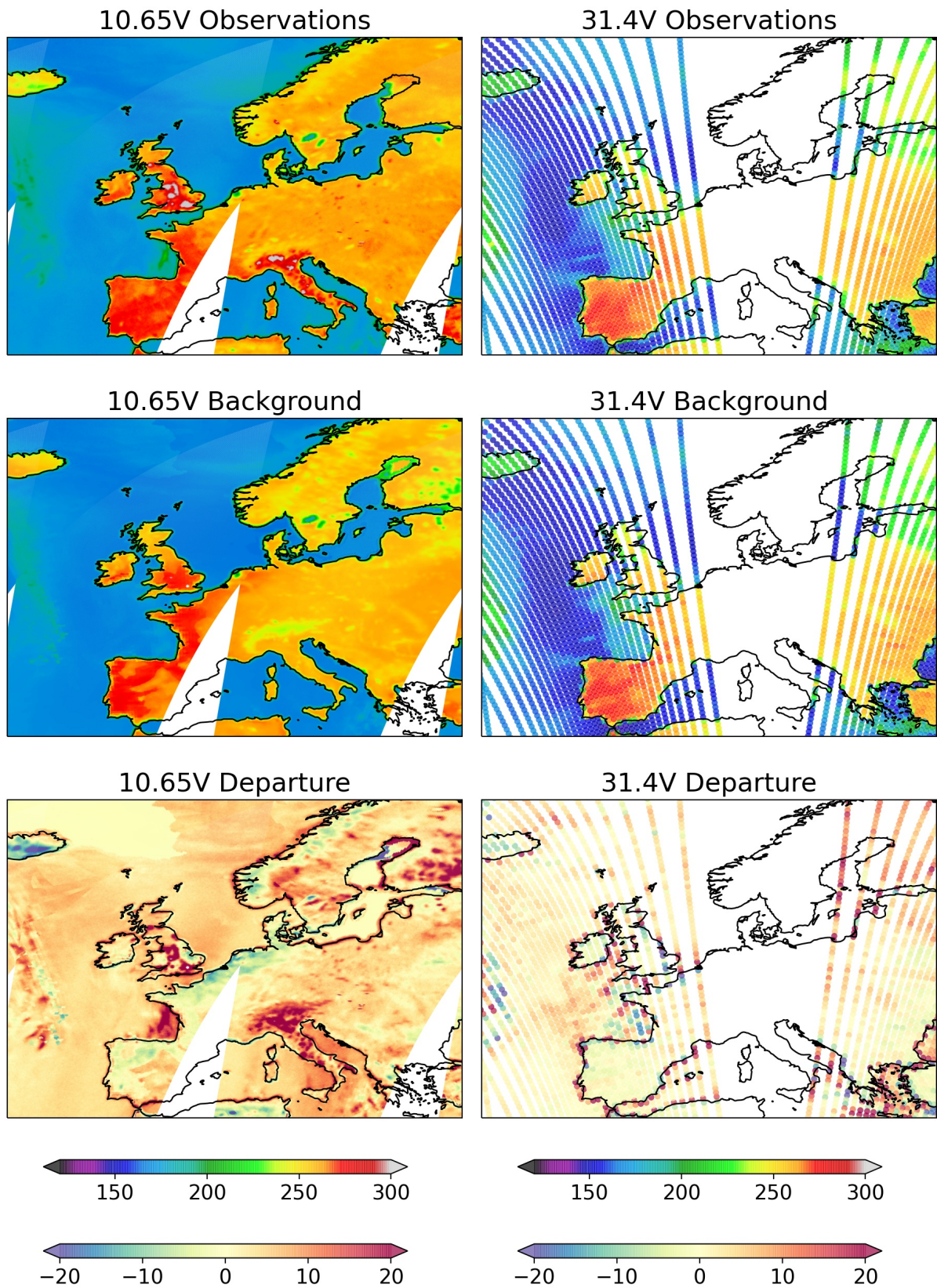
Figure 6: *Observed radiances (top), model background equivalents (middle), and background departures (bottom) from AMSR2 10.65V (left) and Metop-C AMSU-A 31.4V (right) on March 2, 2022 over Europe. These include all scan positions, including those shown to be problematic in Fig. 4.*
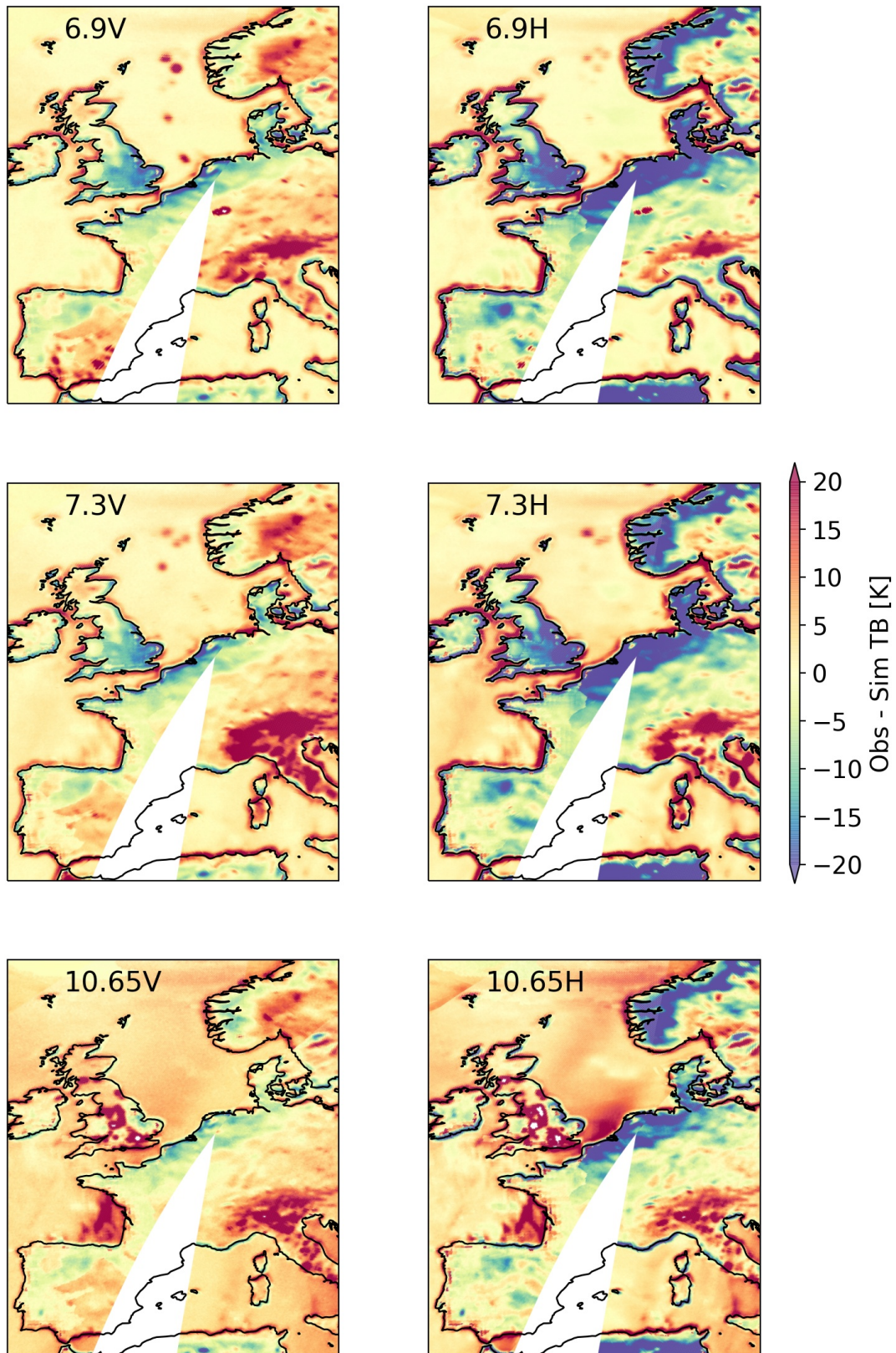
Figure 7: Departures for AMSR2 channels 1-6 on March 2, 2022 over western Europe.

- $T_{2m} < 277K$

- Model sea ice concentration $>= 1\%$

- Land fraction $> 1\%$ and $< 95\%$

- Orography $> 1600m$

- Emissivity retrieval failure or low quality (over land)

- Cold-air outbreak (CAO) screening active (Lonitz and Geer, 2015)

These screening criteria follow the screening choices made for microwave imager frequencies in the IFS. The aim is to avoid known areas of radiative bias in the model, including mountain ranges and frozen surfaces (snow cover and sea-ice). Although coastal areas are currently assimilated at middle microwave frequencies following Geer *et al.* (2022), the choice to screen out coasts is driven more by the low frequencies, which have very large footprints and more significant emission from side-lobes (see Fig. 4 from Draper *et al.* (2015). Scenes where the emissivity retrieval has failed or is using the back-up option of an atlas emissivity are screened out. Lastly, CAO regions have known radiative biases in the IFS due to insufficient super-cooled cloud water in the model, so these are also removed.

Figure 8 illustrates the observations remaining after screening is applied, this time viewing North America. Here we choose mid-range frequencies 18.7 GHz on AMSR2 and 23.8 GHz on AMSU-A. A frontal region of clouds and precipitation is visible east of the United States, showing the characteristic pattern of positive and negative departures side by side, indicative of misplaced cloud features in the model background. Areas over land with near-freezing surface temperatures or high orography are screened out (e.g. northern Canada and the Rocky Mountains) to avoid problematic forward modelling. One fairly clear RFI signal is seen at 18.7 GHz, with positive departures visible around Florida on both sides. This is indicative of reflected RFI off the sea, a well-known feature around the USA coastline at this frequency band.

It is a deliberate decision not to screen out all areas of possible cloud and precipitation, other than the areas of known model bias. This is for several reasons. First, it is the low frequency channels that are the primary concern for RFI, and these are attenuated only by the heaviest precipitation. Second, many of the signals of RFI are expected over land, and attempts to screen out precipitation over land could remove some RFI signals. Third, the distribution of background departures should be relatively Gaussian and centred near zero, even when clouds and precipitation are included; for example, misplaced convective precipitation at 10GHz should manifest as large positive and negative O-Bs side by side, and unless there is a strong model or forward model bias, these should largely balance each other out. Although it is possible to perform analysis on "normalised" departures (O-B divided by the assigned observation errors that are a function of cloud amount), these are tuned for mid- and high-frequency microwave channels rather than the low frequencies, and are a constant term at some channels for non-ocean scenes. So, although analysis of cloud and precipitation contamination could be considered in select cases, the main analysis does not attempt to screen out such scenes.

Lastly, specific to AMSU-A and following analysis seen in Fig. 4, the AMSU-A data will have a further screening applied to remove the outermost 3 scan positions on each side (1-3 and 28-30). This is done routinely for data assimilation due to their strong bias characteristics (Duncan *et al.*, 2022b), and the fact that these radiances are not included in the VarBC minimisation means that they are not adequately bias-corrected. It is thus reasonable to remove these problematic observations here as well because their biases relative to the model background would skew results given our use of bias-corrected departures (Eq. 1).
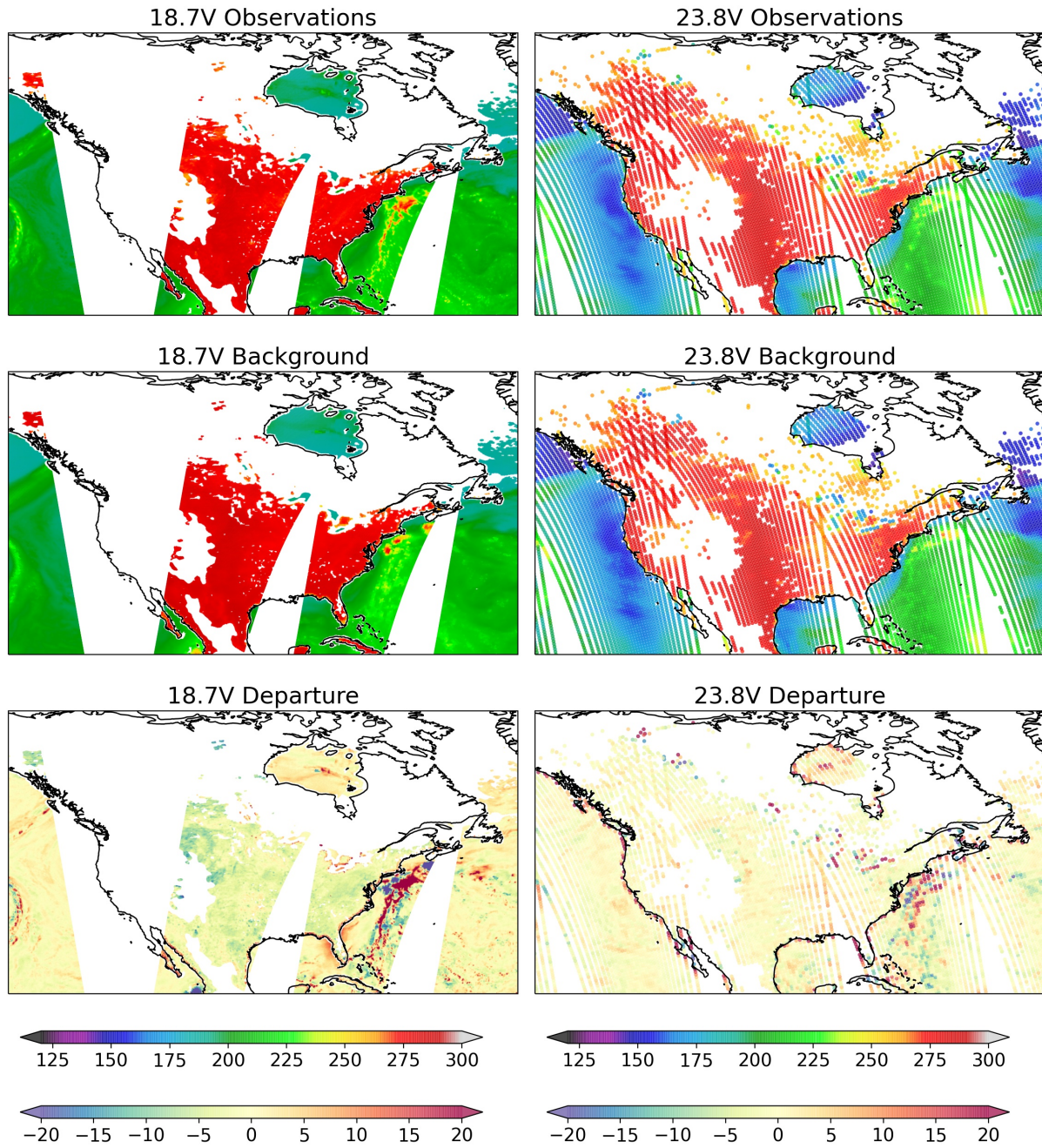
Figure 8: *Showing only observations that have passed the screening criteria, for the 18.7V channel from AMSR2 (left) and 23.8V channel from Metop-C AMSU-A (right). Data from October 2, 2022.*

The main analysis of this project thus applies the screening choices outlined above for all statistical analysis. This is underpinned by the assumptions above regarding clouds and precipitation—namely that such signals manifest as positive and negative departures due to displacement errors in the model, and thus persistent positive departures, even in the vicinity of precipitation, are indicative of possible RFI. Much of the analysis is therefore focused on mean departures over a large data sample. Knowledge of the atmospheric general circulation can then inform whether some signals may be related to atmospheric rather than artificial sources, for example. However, views of the satellite swath and individual radiances are also instructive here, so the following analysis begins with the instantaneous case.

5   Assessment of EORFIScan Screening

Following the geographical distribution of flagged radiances seen in Fig. 2, and the relatively small numbers of total radiances flagged in Fig. 1, it is clear that analysing the full global sample of radiances at once would result in diluted statistical signals. To combat this, the analysis will centre on regions with known RFI contamination at multiple bands.

Before looking at any composite, statistical analysis, we can examine the two orbits shown over Western Europe in Fig. 7 and assess visually how the possible RFI features are matched by the flagged points from EORFIScan. This is shown in Figure 9, where only points that are flagged as medium- or high-confidence RFI are shown. It is clear that most points flagged as potential RFI exhibit positive departures, with mostly red colours displayed and very few negative departures seen at all. At 6.925 and 7.3 GHz, the algorithm picks up blobs of strong positive departures in the North Sea that are quite likely RFI as discussed above. The urban parts of the UK with strong positive departures at 10.65 GHz are identified at both polarisations, as are urban areas of Italy. At 10.65 GHz there are also large areas over sea where EORFIScan is picking out possible reflected RFI. This visual inspection of comparing Figs. 7 and 9 indicates that EORFIScan is picking up the most obvious features from the departures, with impressive specificity for the different channels and polarisations.

To see how the departure map looks with all flagged radiances removed, see Fig. 10. Comparison of these two figures shows that many of the clear RFI signals that could be visually identified have been removed by the flagging. It is rather conservative, however, in the vicinity of coastlines, with a large buffer between the patch of reflected RFI and the coasts of eastern England and the Netherlands. This is clearest near Gibraltar, where comparison with the previous figure shows a rather wide area of reflected RFI but here only a thin slice of observations are flagged. It is also conservative on the periphery of potential RFI sources, as can be seen in the North Sea at 7.3 GHz or in the Bay of Biscay at 10.65 GHz, where some RFI has been removed by the flagging but perhaps more could be screened out. In the latter case this is hardly clear from the departures alone, as it seems likely that precipitation signals and RFI are both present in this region. The overall impression from this figure is that a lot of likely RFI is being identified by EORFIScan, though the balancing of false positives with identification is most difficult near coastlines and precipitation, particularly for lower levels of contamination.

Moving to the statistical analysis, first we will examine a region comprising North America and Europe, as this region contains known RFI sources at several frequencies of interest. Second, the analysis moves to a region covering the Middle East and southern Asia. Then we will examine the efficacy of different flag levels provided by EORFIScan, followed by some specific analysis of reflected RFI over sea as seen by AMSR2.
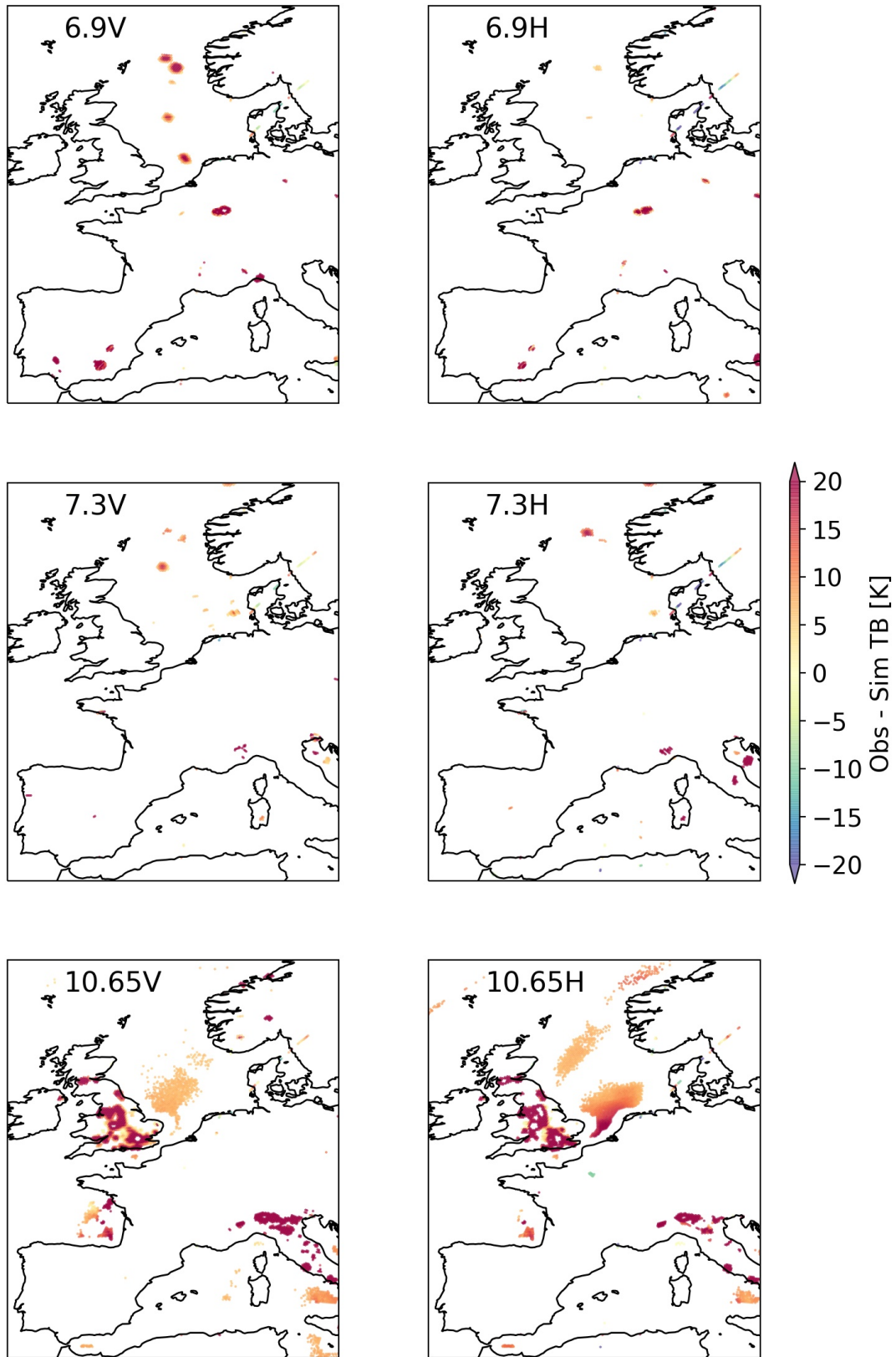
Figure 9: Departures for AMSR2 channels 1-6 on March 2, 2022 with RFI-flagged data shown only (medium- and high-confidence). Note that no IFS screening has been applied.
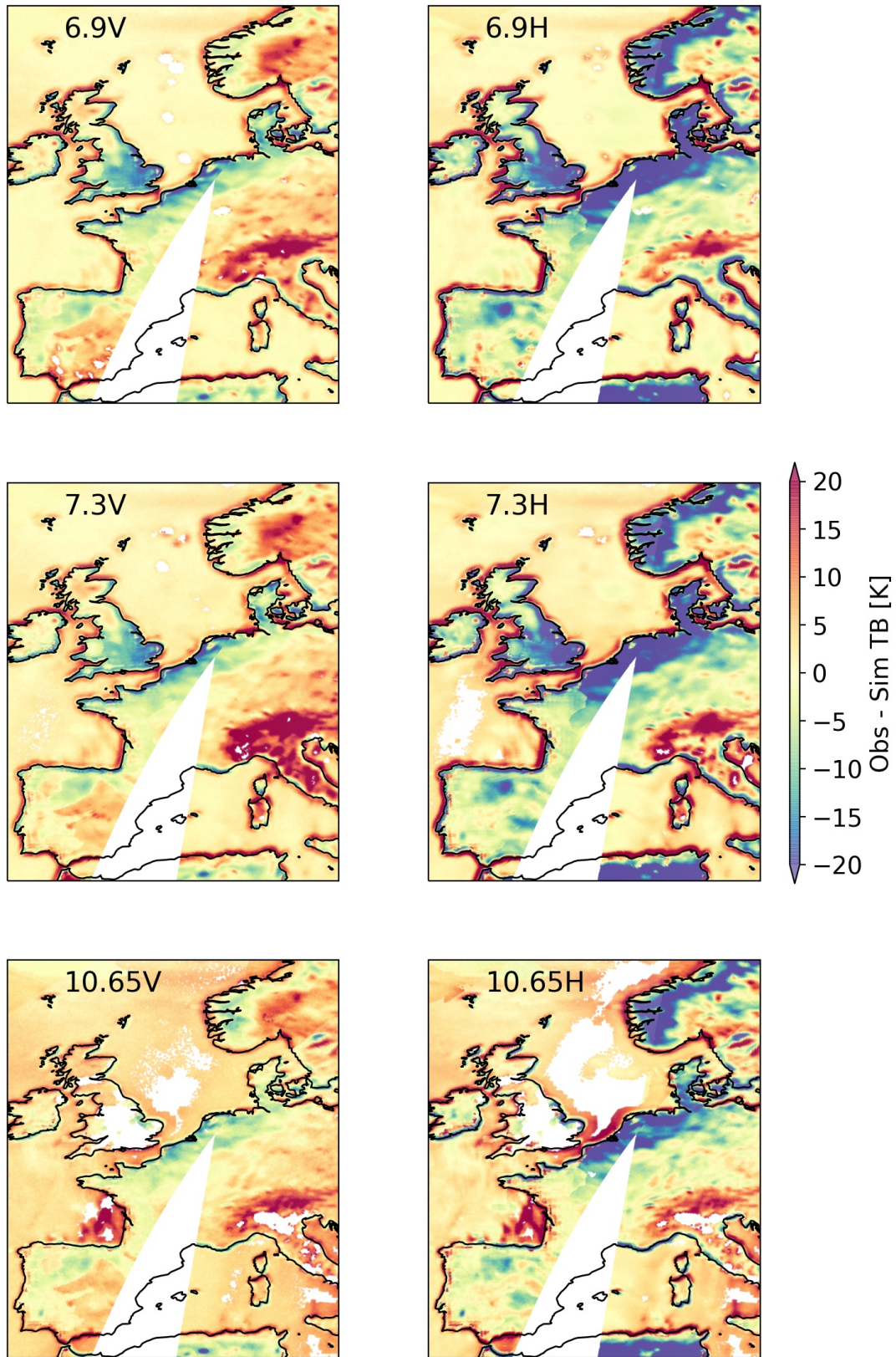
Figure 10: As Fig. 7 and 9, but with flagged data of any confidence level removed (i.e. low, medium, and high). Note that no IFS screening has been applied.

5.1 North America and Europe

First, we will compare the mean departures of all screened observations and the mean departures of flagged observations only. Figures 11 and 12 show monthly mean departures for most of the AMSR2 V-pol channels, covering March 2022 on a 1 degree grid. Flagged observations should exhibit net positive departures, and thus consistently identified RFI should appear as mostly red areas in the bottom panels for each channel. This is indeed what is visible for the lower frequencies in most circumstances, with 6.925 and 7.3 GHz flagged data identifying generally positive departures over land in particular, with many urban areas standing out. Some areas of RFI are clearly visible in the mean map for all data, surely with frequent and/or intense interference present to manifest in the monthly mean departure. Such areas include Southern California, Atlanta, and an area near Luxembourg at 6.9V; Morocco, Ukraine, and Italy at 7.3V; England, Cairo, and Italy at 10.65V.

At 18 GHz and higher, the only large-scale, clear signal of RFI is the reflected RFI ringing the United States' coastline at 18.7 GHz. Although some areas are flagged at 23.8V and 89.0V, no consistent signals of RFI are seen in the departures. Some likely weather signals are visible in the north Atlantic for 23.8V. These are likely to be weather signals due to the similar structure of flagged points at 18.7V as seen in the figure, and the lack of known sources in this vicinity. At 89.0V the only larger area with significant flagging is near Baja California, but the departures are consistently near-zero here, so this seems not to be RFI. Some smaller features may warrant further investigation as to possible sources, such as the potential RFI seen north of the Iberian peninsula at 18.7V, or the small area of positive departures flagged near the coastline of Washington DC at 89V.

Figure 13 shows three sample channels from AMSU-A, giving the same view as for AMSR2 but with a zoomed-in colourbar to emphasise smaller mean departures and lower thresholds for plotting a grid point, as AMSU-A has far lower data density than AMSR2. These panels show that the main areas of positive biases are coastlines for 31.4 and 50.3 GHz, possibly because a footprint-specific land fraction is not yet available for AMSU-A in the IFS (in contrast to imagers). A few of these coastal areas are flagged as potential RFI, but it is hard to verify whether these observations along the coastlines are likely RFI as we see blue and red side by side in most regions. One other region of interest is off the coast of the Florida Panhandle, where a mean positive bias of maybe 2-5K is visible at 31.4V. This region is not flagged by EORFIScan and exhibits a similar but weaker bias at 50.3 GHz, so this may simply be an area of systematic low cloud bias (i.e. not enough liquid cloud) in the IFS. A similar feature is seen near Gibraltar. No clear signals of RFI are visible at 52.8 GHz and higher frequency channels on AMSU-A.

Another way to analyse the RFI detection is via a histogram of departures. We assume that precipitation signals and random errors of cloud displacement and such will be symmetrically distributed around zero to first order, whereas RFI signals are expected to add to the positive tail of the distribution. Thus skilful RFI detection should pick out a significant amount of this positive tail for an RFI-affected channel and region. Using the same region as analysed above, Fig. 14 shows the lowest eight channels from AMSR2, with radiances split into groups covering land and sea[9]. For most channels shown, the histograms are much wider for observations over land, whereas for data over sea they are narrower and most are centred near zero. However, as we would expect with RFI sources present, most of these histograms exhibit some asymmetry. For example, 6.9V exhibits a larger positive tail over land and sea, with roughly as many +40 K departures as -20 K, and several greater than +50 K with no such negative departures seen. These long positive tails are more distinct for the lowest frequencies, which have less sensitivity to hydrometeors but also generally witness more RFI.

---

[9]Land is defined as $> 95\%$ land fraction within the radiance FOV, with sea defined as $< 1\%$. Note that as this is channel-dependent, the sample is different for different frequencies.
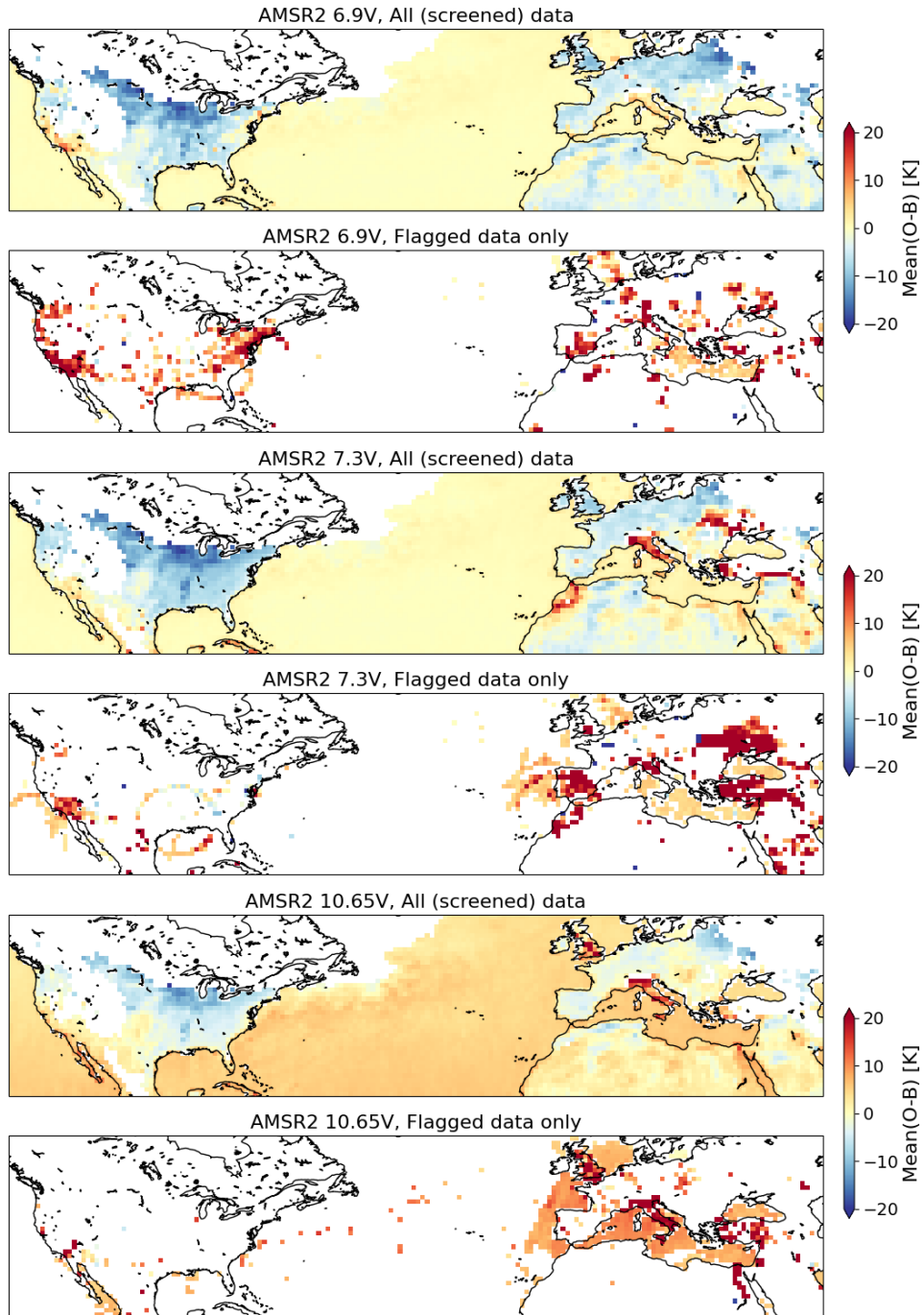
Figure 11: Mean departures from AMSR2 channels 6.9V, 7.3V, and 10.65V comprising data from March 2022. Plots alternate between all screened observations (top) and flagged observations only (bottom). At least 1000 (screened) observations need to exist in a grid box for it to be plotted, and at least 10 flagged observations for the bottom panels.
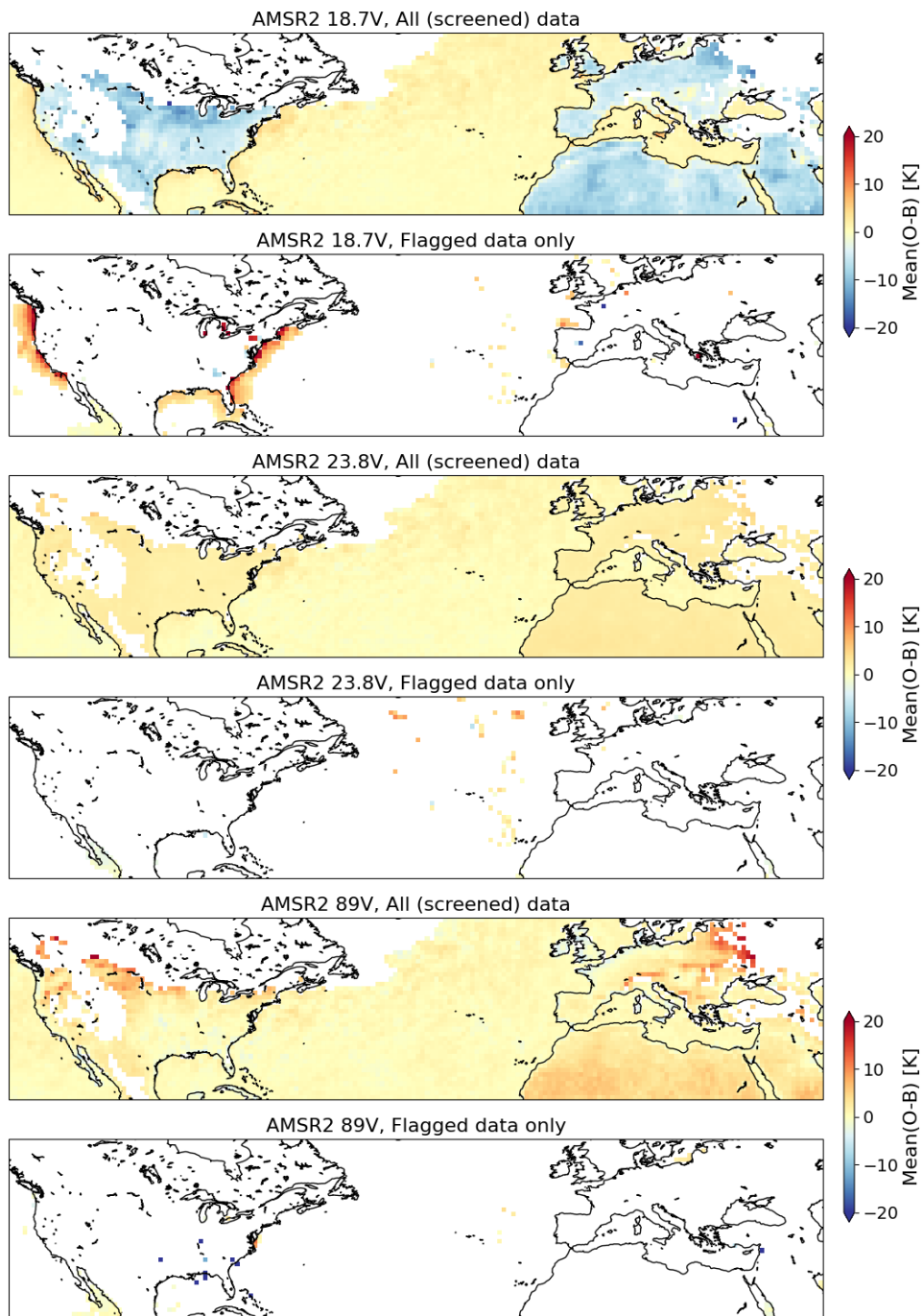
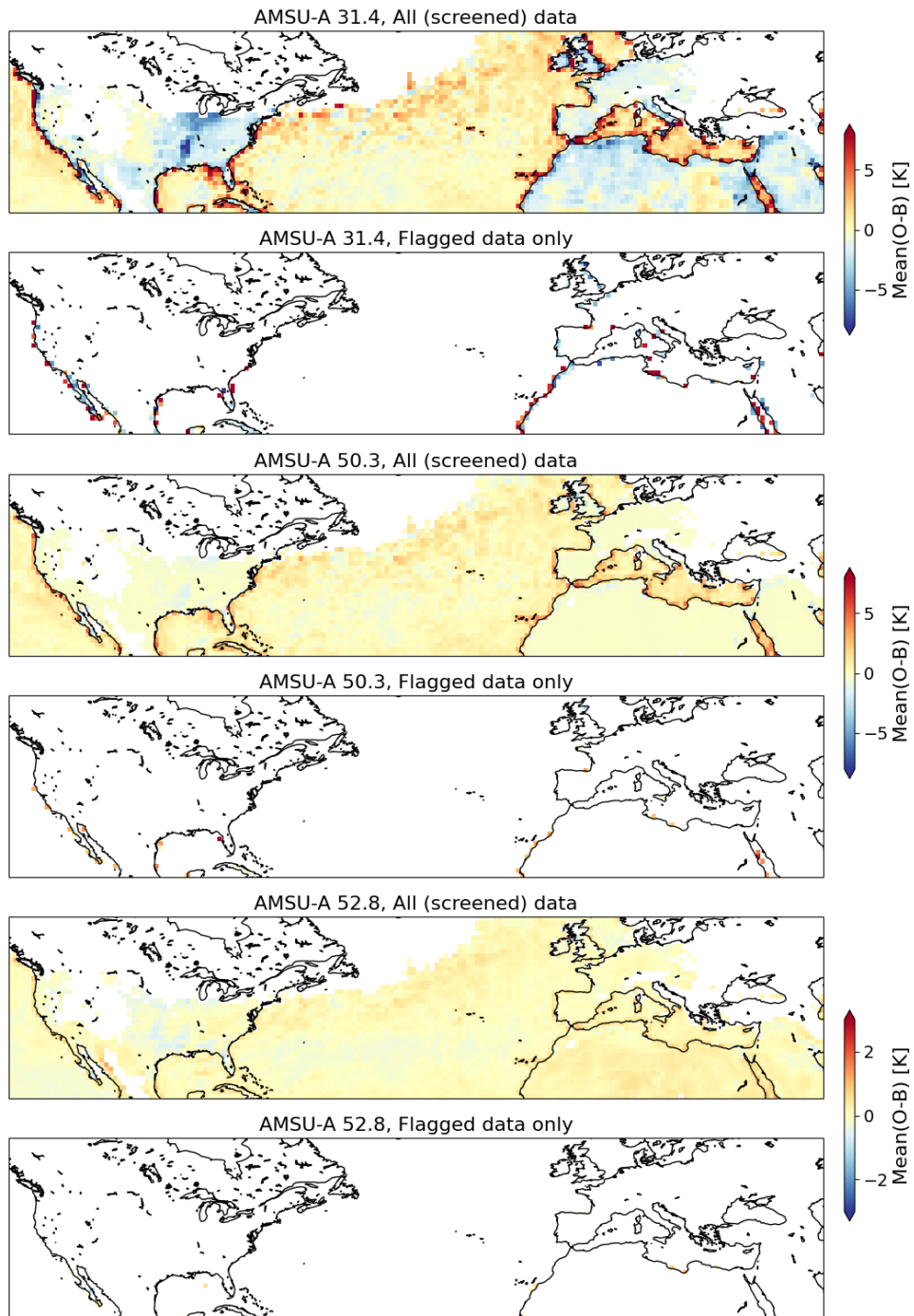*Figure 12: As Fig. 11, but for 18.7V, 23.8V, and 89.0V channels.*

Figure 13: As previous figures but for AMSU-A channels 31.4V, 50.3V, and 52.8H channels. Note the smaller colour bar ranges. For points to be shown here they require 50 observations (5 for flagged) due to the much lower data density of AMSU-A relative to AMSR2.

If relative symmetry of the departure histograms around zero is assumed for an RFI-free channel, then one could quickly surmise that there is little to no RFI over land at 18.7 GHz, for example. This indeed largely matches what EORFIScan tells us about RFI at 18.7 GHz, with the main global source being the coastline around the USA. The EORFIScan algorithm does mostly identify positive departures over sea as potential RFI for 18.7V and 18.7H. At the lower frequency bands where many of the large departures may be due to RFI, we can see the solid and dotted lines converging, indicating roughly where EORFIScan thinks that all such large departures are caused by RFI. Crucially, this is not the case for 10.65 and 18.7 GHz, where large positive departures are more plausibly associated with heavy precipitation.

In case the logarithmic scale of Fig. 14 is hiding any details, we can view the fraction of observations flagged as RFI as a function of departure bin in Figure 15. This shows that for the 6.9V and 7.3V over land and sea, large departures of +30 K are flagged a majority of the time. A similar high fraction for large positive departures is seen at 10.65V over land. The EORFIScan algorithm appears to be more cautious for low-frequency H-pol channels, with lower fractions of large positive departures flagged at 6.9H, 7.3H, and 10.65H. In an interesting contrast with the lower frequencies where more V-pol data is suspected RFI, EORFIScan flags a higher percentage of 18.7H points over sea than 18.7V. A peculiar feature in this set of plots is the fraction of 10.65 GHz radiances flagged for RFI over sea, which shows a relatively small peak at about +10 K departure. It is not immediately clear why this peak in flagged fraction is so limited for 10.65 GHz over sea specifically.

Lastly, what does the removal of all flagged data mean for the most commonly used metric of departure analysis in NWP, the standard deviation of departures? Figure 16 shows the monthly average standard deviation of departures for all data and the sample with no flags set. The difference of the two plots indicates how much the removal of flagged data points can clean up the monthly mean variability of departures. In most areas there is not a large difference, but if using the previous figures as a guide, one can see the decrease in std(O-B) over locations such as England, Italy, Ukraine, the North Sea, and so on. For the most part, areas of larger natural SST variability and precipitation appear unaffected by removal of the flagged observations.

5.2 Southern Asia

Moving to a different region, Fig. 17 provides the same information as Fig. 11 but for an area encompassing the Arabian peninsula, India, and east to Japan and the maritime continent. In this region the flags are primarily picking out positive mean departures again, with numerous sources seen. For example, we see clear examples over India at 6.925V, Saudi Arabia and Southeast Asia at 7.3V, and Japan at 10.65V.

One motivation to examine this region was to disentangle potential RFI near the Arabian peninsula, as this part of the Arabian Sea (and to a lesser extent the Bay of Bengal near Bangladesh) is flagged at several frequency bands, a little like the area near Baja California mentioned earlier. However, the mean departures do not give clear evidence of RFI at most of the frequency bands studied, and so it is hard to corroborate the existence of RFI in these areas. There appears to be no RFI contamination at 18.7 GHz and higher frequencies (not shown), and none at 6.925 GHz either. Some limited flagging is present at 7.3 GHz in the Arabian Sea, but departures of the flagged data are only slightly larger than for all data. Similarly, at 10.65V we see mean departures only slightly higher than the model average in the flagged data sample, making it difficult to corroborate this signal as RFI. It is noteworthy that these regions are not as frequently flagged in October 2022 (see Fig. 23 in Appendix), so it is possible that some transient phenomenon such as abnormally warm SST is to blame for these features.

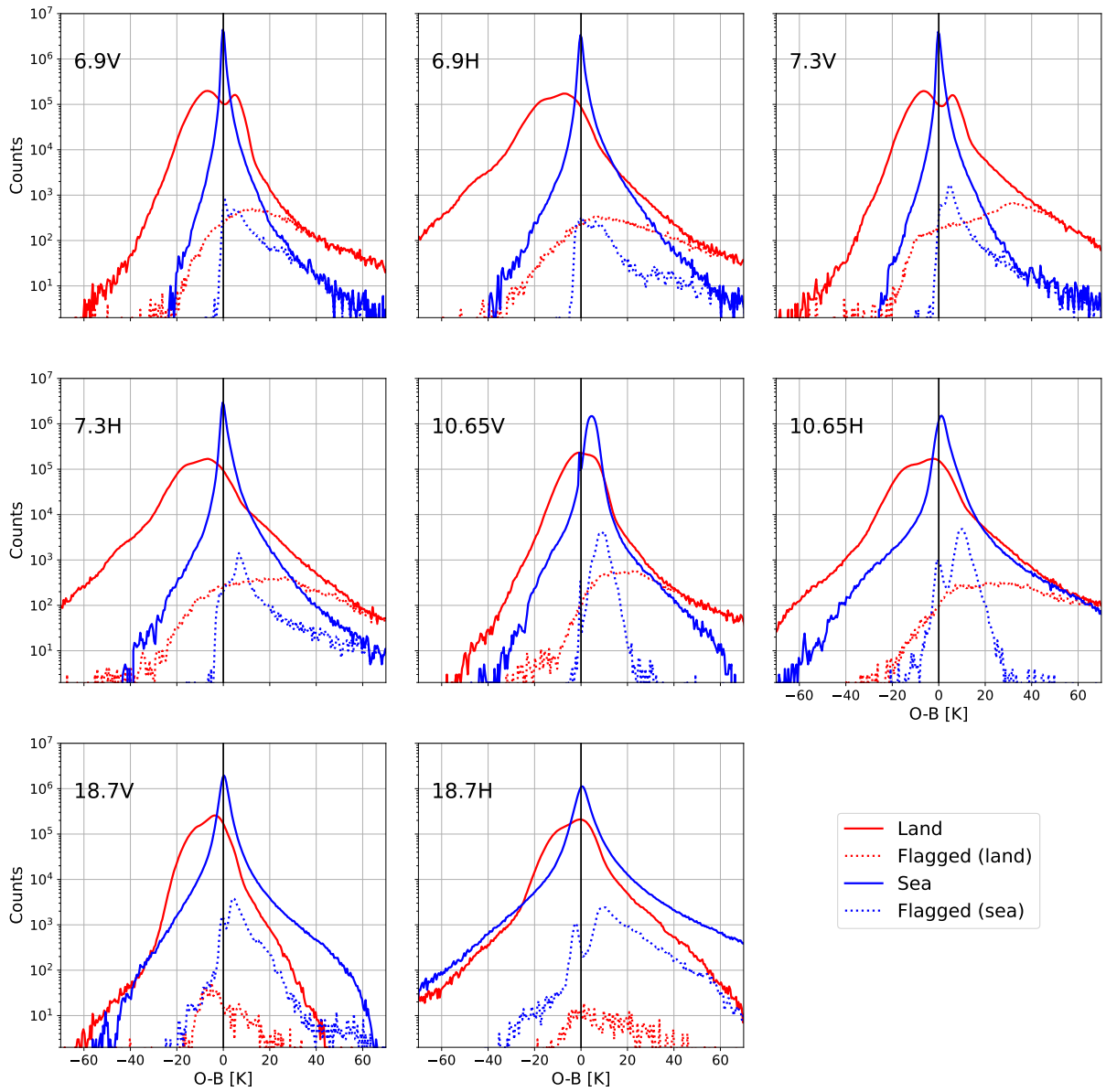Another area of interest concerns the regions of RFI identified in the East and South China Seas at 6.925

Figure 14: Histograms of departures for screened observations over land (red; > 95% land fraction) and sea (blue), comprising data from March 2022. The histograms of all points are given by solid lines, with the flagged histograms given by dotted lines. Region is the same as for previous figures, covering North America and Europe.
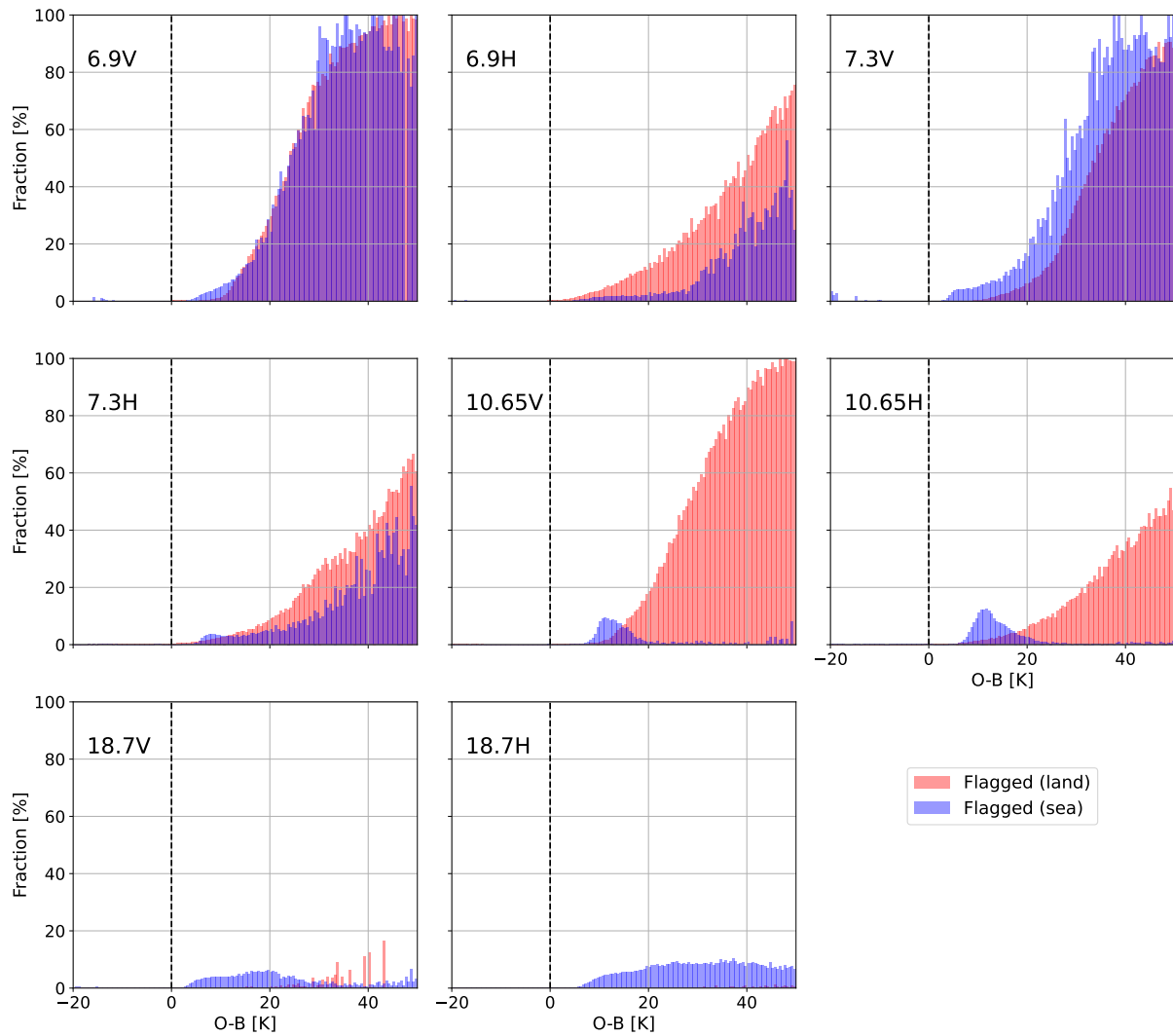
Figure 15: As Fig. *14*, but showing the fraction of total radiances flagged as a function of departure bin.
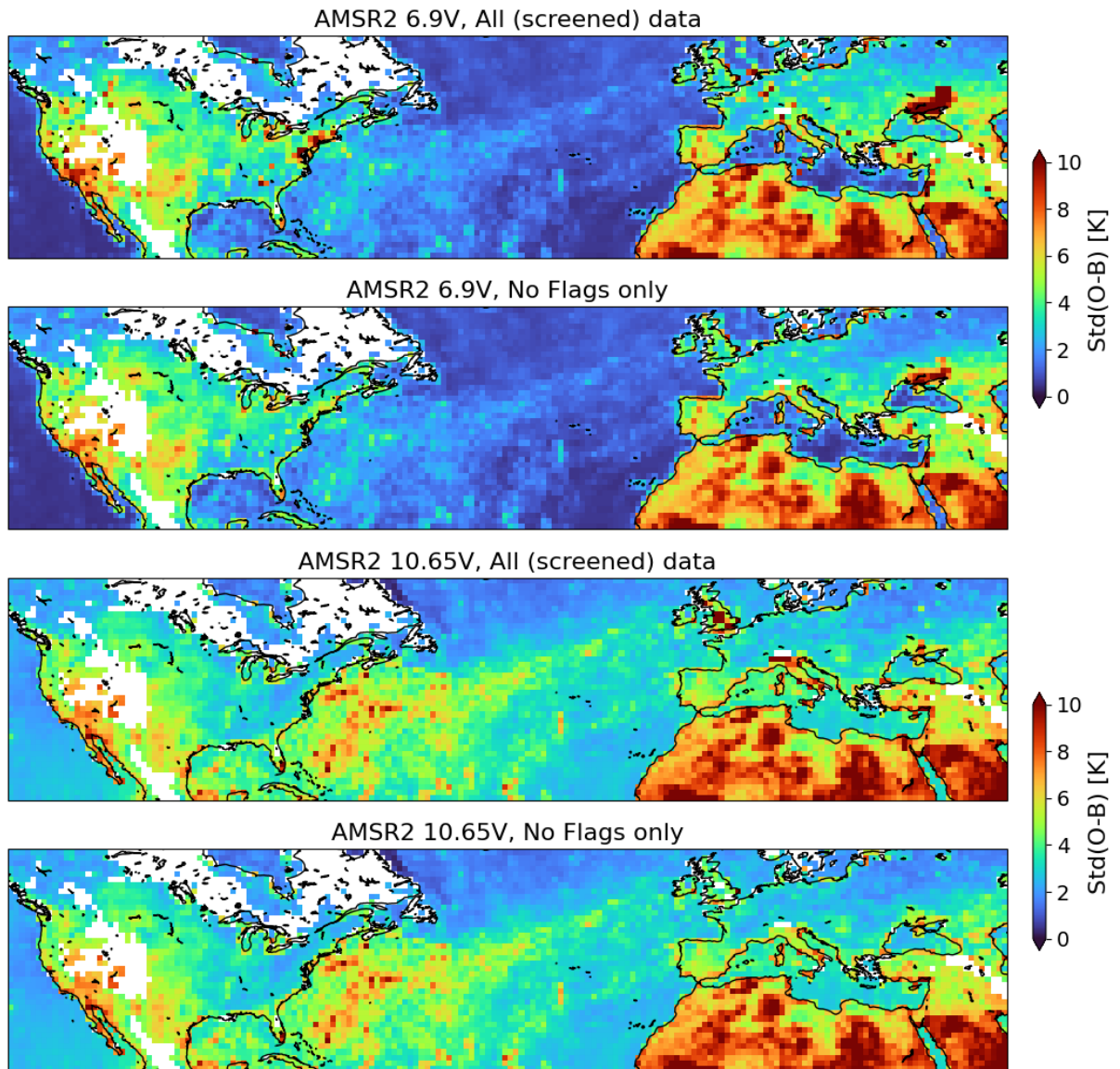
Figure 16: *Standard deviation of departures for all screened observations (top) and just observations with no flag (bottom) from AMSR2 channels 6.9V and 10.65V, comprising data from October 2022. At least 1000 (screened) observations need to exist in a grid box for it to be plotted.*
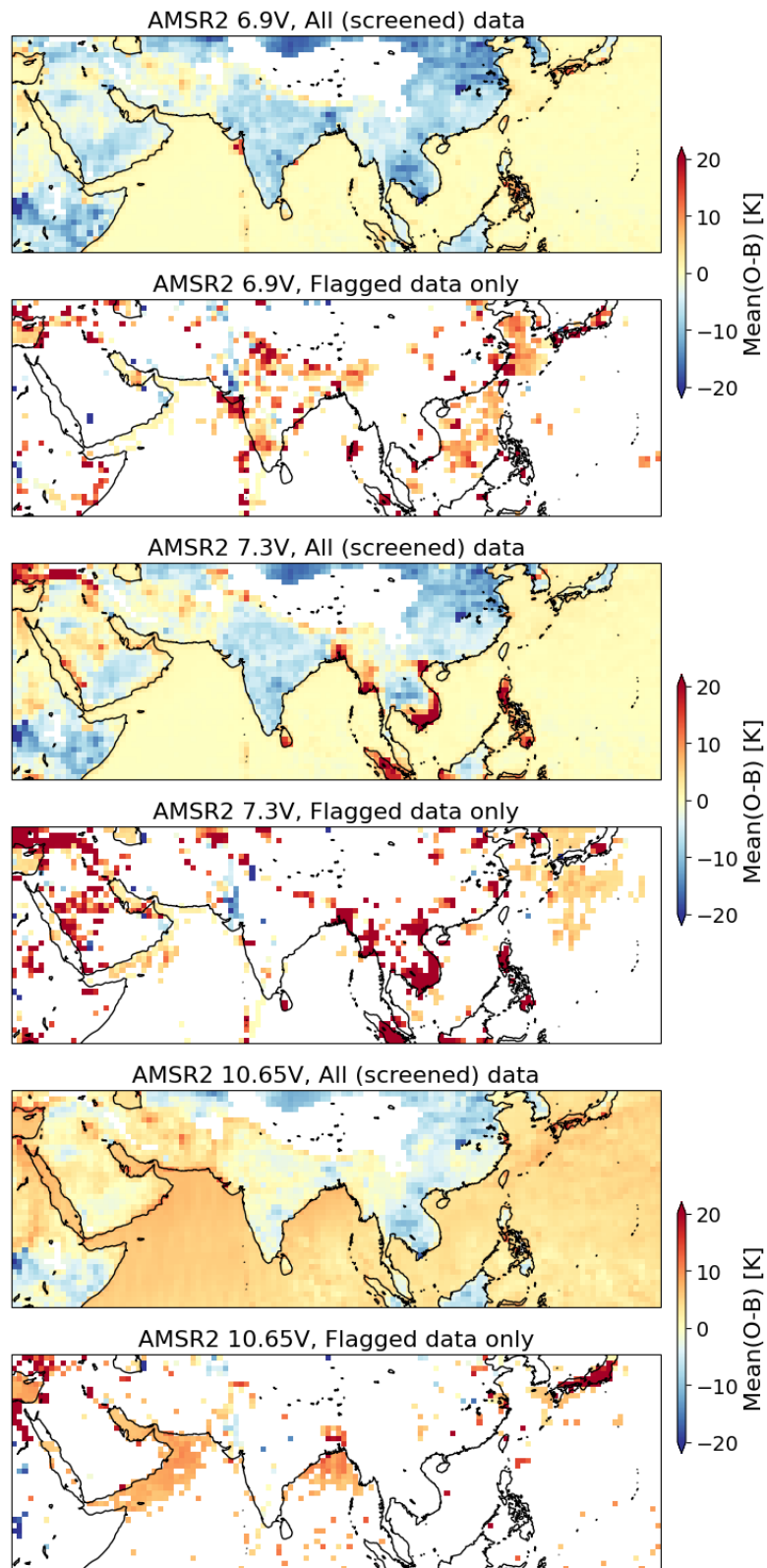
Figure 17: Mean departures for all screened observations (top) and just flagged observations (bottom) from AMSR2 channels 6.9V, 7.3V, and 10.65V comprising data from March 2022. At least 1000 (screened) observations need to exist in a grid box for it to be plotted, and at least 10 flagged observations for the bottom panels.

GHz. Even in the sample with all data, this area has slightly elevated mean departures at 6.9V and 6.9H, and the data flagged indeed exhibit larger positive departures in this region in both the March and October 2022 time periods. This may be a new finding, as Wu *et al.* (2020) was clear in stating that this region experiences RFI at 7.3 but not 6.925 GHz. It appears, however, that much of the signal is near the 5 K detection limit from that study, so it may have been missed in this earlier work. It is unclear where this interference could be coming from, but such low-level but widespread interference at 6.9 GHz is the most problematic for assimilation. This could especially be an issue in the case of typhoons in this region, for example, as more RFI-affected data would make it past quality control procedures in precipitating conditions due to a larger assigned observation error.

5.3 Flag Levels

The analysis thus far has focused on data flagged by EORFIScan as medium- or high-confidence RFI. However, the algorithm provides four different flag levels for all radiances—none, low, medium, and high (Sec. 3.2). In Figure 18, the histograms of these four flag levels are given for the lowest eight channels on AMSR2, again using the regional domain encompassing North America and Europe. Here we are just focusing on data over sea (see the plots for land data in Appendix). The histograms with all flagged data removed (No Flag) are indistinguishable from the full histogram for several channels because not so much data is flagged as a total fraction. However, for the V-pol channels 6.9V and 7.3V these flag-free histograms are indeed more symmetric around zero, significantly reducing the departures of +20 K and more. These two PDFs still have a longer positive tail than would be expected with an unbiased model and observation operator, but are substantially improved. The H-pol PDFs are not as impacted, as suggested by the earlier discussion of the fraction of large departures flagged in Fig. 15. Similarly, RFI flagging at 10 GHz over sea does not appear particularly skilful at identifying clear RFI, with a large positive tail remaining and most suspected RFI confined to departures between about 0 to +15 K at both V- and H-pol.

Most of what we could call the clear false positives, i.e. flagged data with a departure that is negative or near zero, are limited to data in the low confidence category of flagging; the logarithmic scale rather accentuates these cases, but it does not appear that false positives are a large concern even for the low confidence flagging in this analysis. In the worst instances over sea, these clear false positives account for less than 1% of data, and for many channels the low confidence histogram for near-zero departures is 2.5 to 3.5 orders of magnitude lower than the histogram containing all points.

The different classifications of RFI confidence appear to be useful for a potential user of the flags. The strongest RFI is indeed identified by the high confidence category, with larger amounts of data identified in the lower confidence categories leading to more apparent false positives. This type of information could be useful in an assimilation context when deciding pre-screening of observations, for instance.

5.4 Reflected RFI

To focus on the specific issue of reflected RFI over sea, we can use the orbit of AMSR2 (with its ascending node at 13:30 and descending node at 01:30 local time) to isolate signals that could be reflected signals from satellites in geostationary orbit. Reflected RFI over sea is a known issue for 10.65 and 18.7 GHz around Europe and North America, respectively (Draper, 2018). If we split the AMSR2 data into ascending and descending nodes, we would expect that the reflected signal from geostationary direct broadcast satellites manifests only on the descending nodes, as these provide the right glint angle conditions given the AMSR2 forward-pointing view geometry.
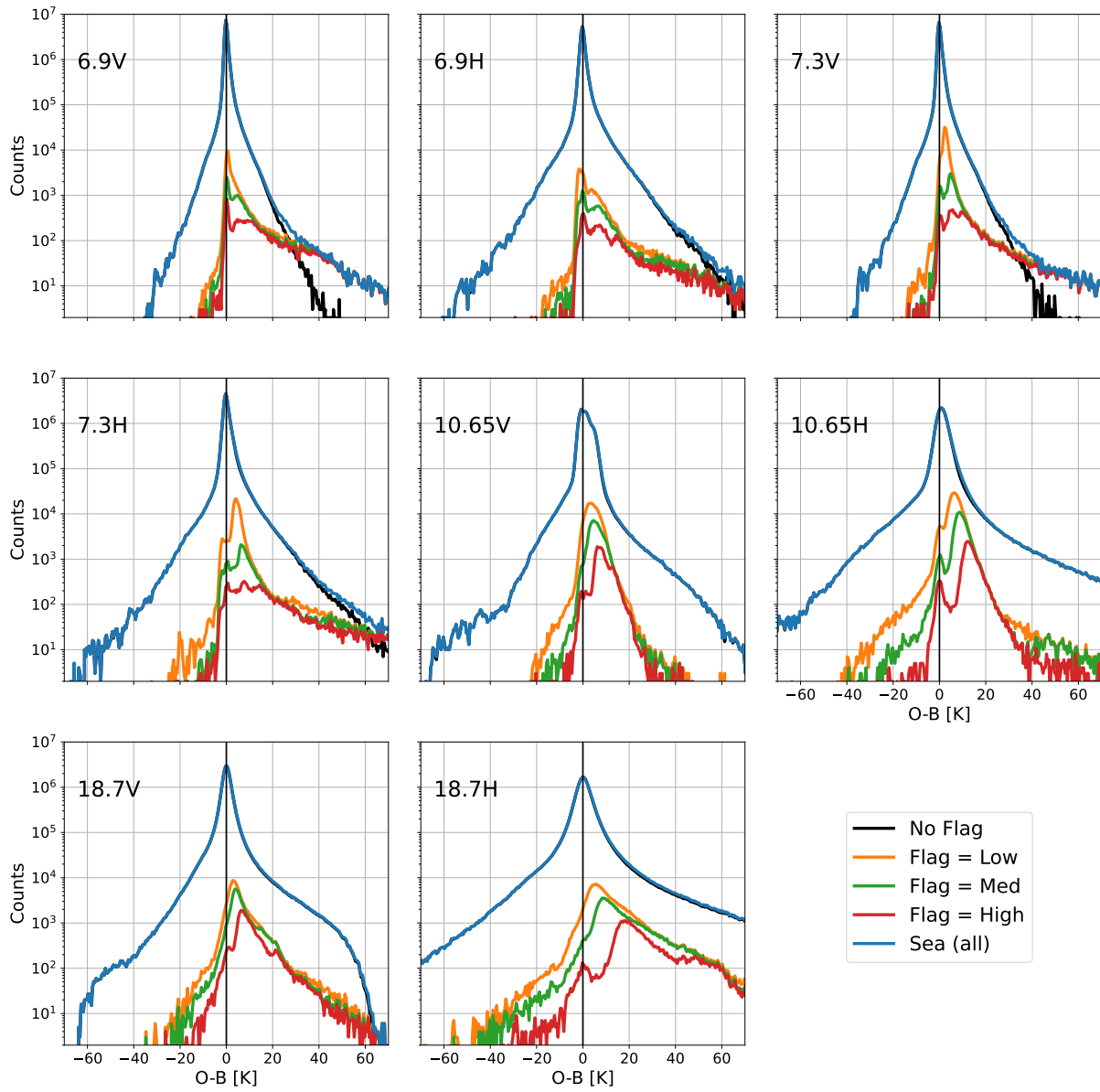
Figure 18: Histograms of departures for screened observations over sea from October 2022. The region is the same as for previous figures, covering North America and Europe. Note that here the low and medium confidence levels are inclusive of higher confidence levels to show histograms that don't overlap.
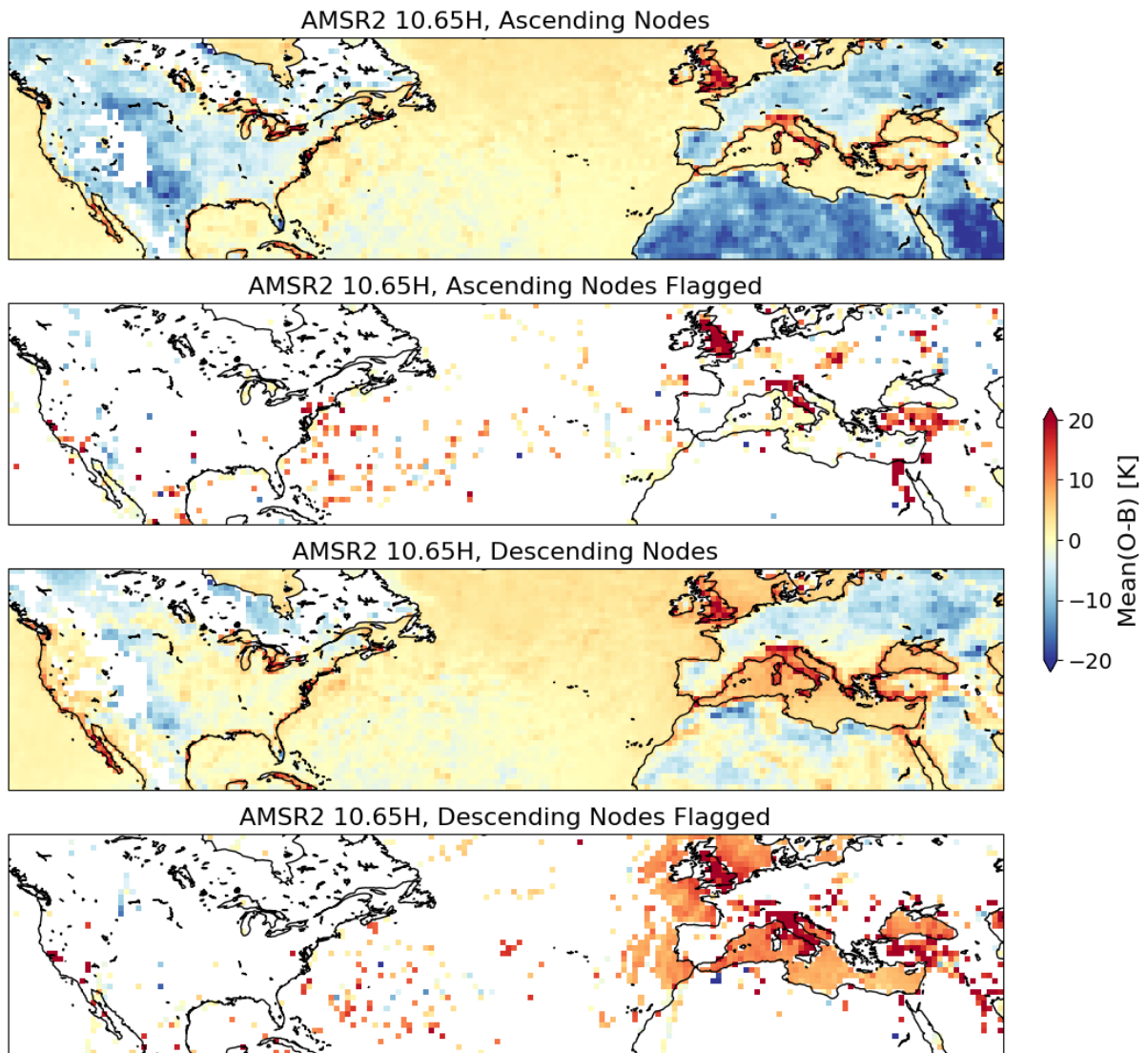
Figure 19: Mean departures for all screened data at 10.65H channel in October 2022, separated into ascending (top) and descending (bottom) nodes. Flagged data only are given in the second and fourth panels.
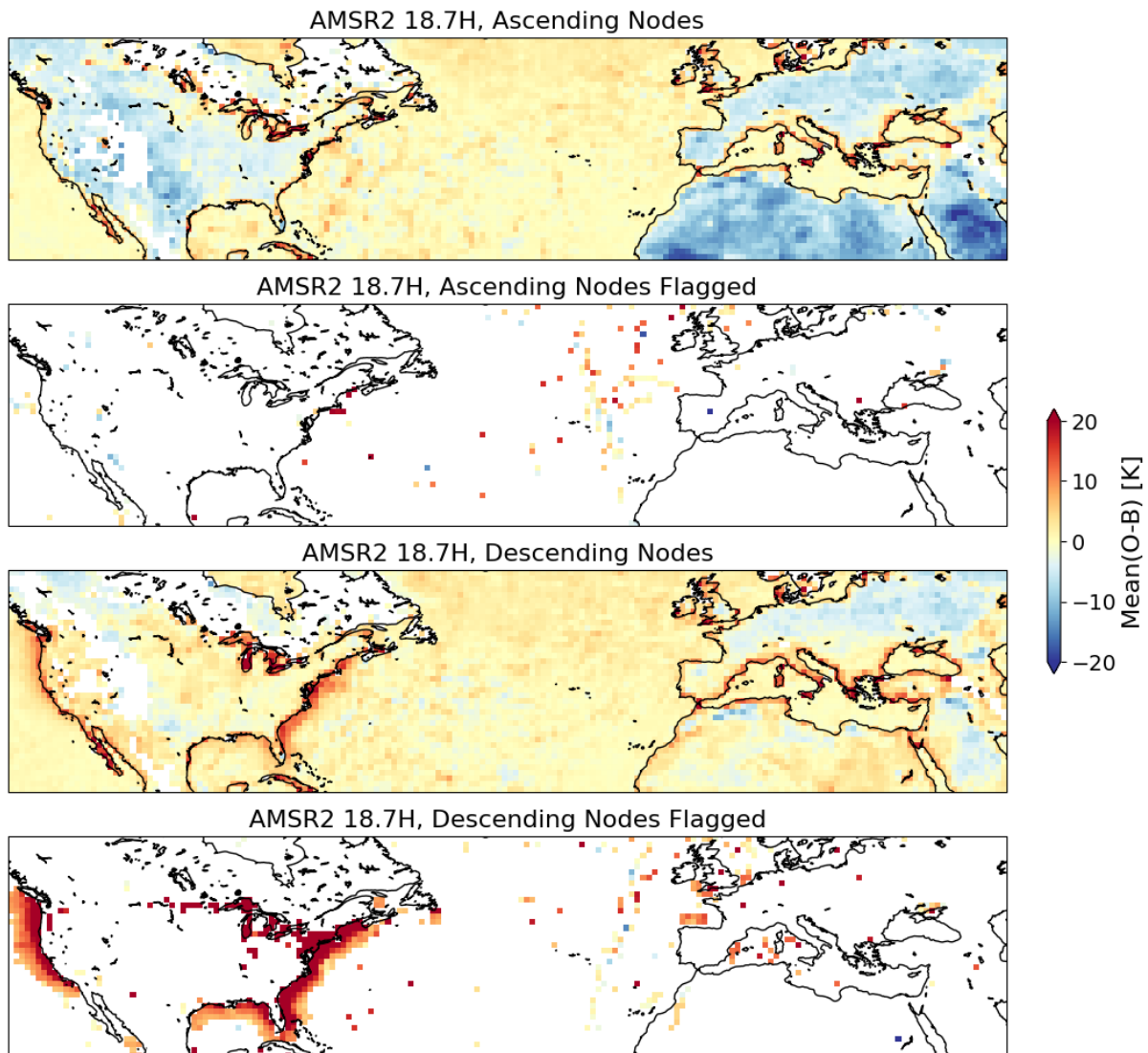
Figure 20: As previous figure but for the AMSR2 18.7H channel.

Figure 19 shows the North America and Europe with the same mean departures on a 1 degree grid as presented earlier. Now the top two panels are for ascending nodes only, with the bottom two panels giving descending nodes only. Here the H-pol channel is shown, but patterns are quite similar for both polarisations; we are showing data from October here, but again the patterns are very similar over sea in March as well. EORFIScan is indeed only flagging RFI over sea in the waters around Europe on the descending nodes. Interestingly, some of the RFI sources over land exhibit differences in detection between nodes that are likely not associated with reflected signals. For example, RFI in the Nile valley is much more prevalent in the ascending nodes, whereas Western Europe sees more RFI at 10.65 GHz in the descending nodes. The causes for this are not obvious and could differ on a source by source basis, for instance with a source active during the daytime (13:30 local time) but not the middle of the night (1:30).

The same view is given for 18.7H on AMSR2 in Fig. 20. Again this clearly shows that EORFIScan is picking out the reflected RFI on descending nodes around the USA coastline, with effectively no data
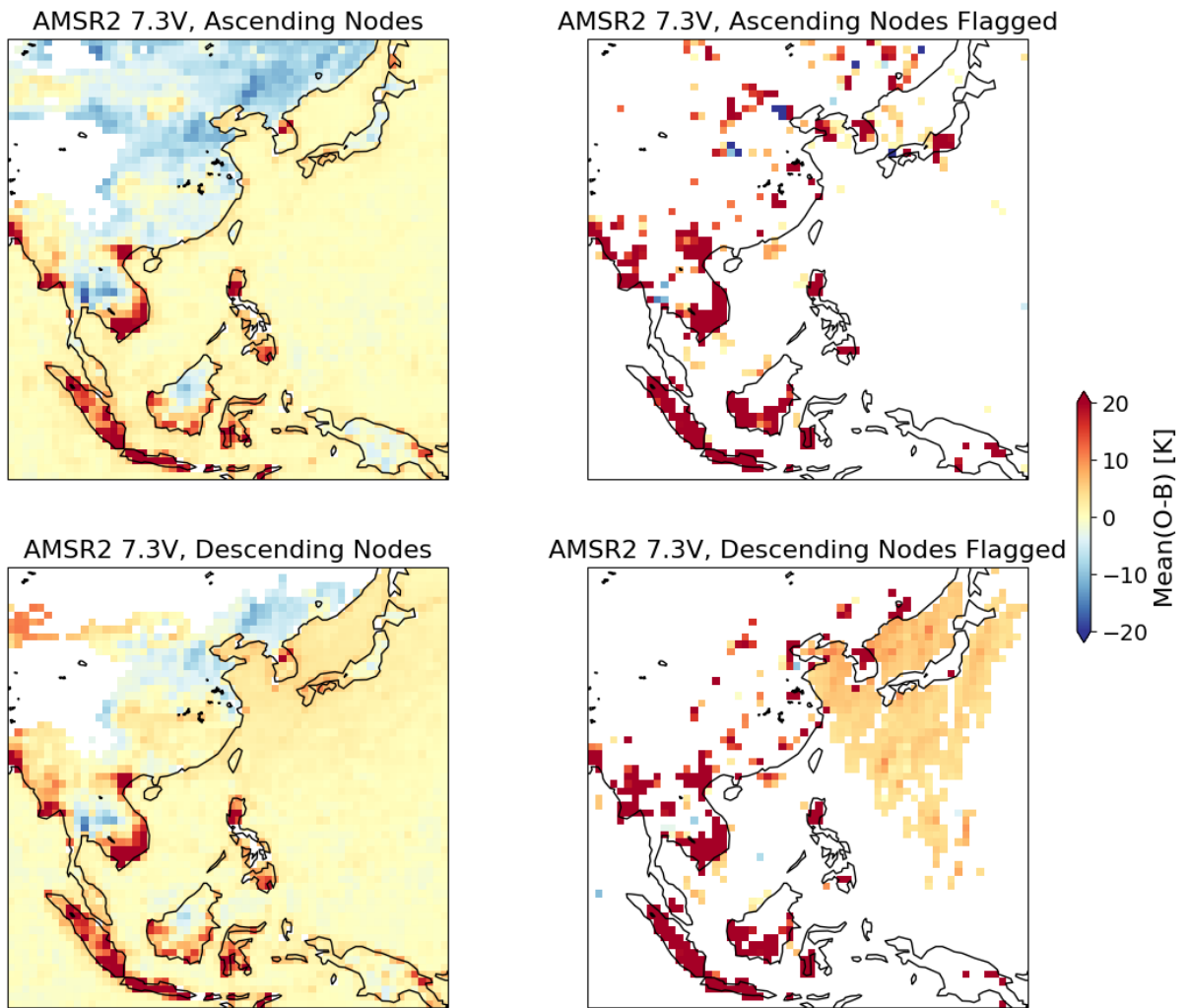
Figure 21: As previous figures but for the AMSR2 7.3V channel over East Asia.

flagged in the same areas on ascending passes of the satellite. In addition to the coastline periphery, significant RFI is seen across the Great Lakes and parts of the densely populated east coast. The Great Lakes RFI is presumably also reflected interference, as seen along the coastlines. As with 10.65 GHz, the H-pol channel is shown here, but the pattern for 18.7V is almost the same. One other area to note is west of France, where we see two smaller patches of RFI identified just north of the Iberian peninsula and off the southwest coast of Britain. These signals are not frequent but are associated with positive mean departures both in October and March, so this may be an area to keep an eye on for interference in the future.

Lastly, the same points can be made for the 7.3 GHz channels on AMSR2 near the seas around Japan. Figure 21 illustrates the reflected interference that is picked out by EORFIScan in the descending nodes at 7.3 GHz, a signal that was previously identified by Wu *et al.* (2020). These signals are relatively widespread in the seas around Japan and Korea, and clearly identified by the flagging as a reflected signal. The reflected signals shown here at at V-pol, but they are present in the same locations and with a stronger magnitude at H-pol as well. This orbital analysis also seems to indicate that the small area of 7.3 GHz RFI seen off the coast of Hong Kong is likely not a reflected signal, as it is present in both ascending and descending orbits with similar magnitude mean departures.

6 Conclusions

This study has leveraged the all-sky microwave radiance assimilation at ECMWF to assess the pressing issue of radio frequency interference at commonly observed radiometry bands. Its immediate conclusions are limited to the scope of this project, which aimed to assess externally-produced RFI identification with a state-of-the-art NWP system. Here we will first discuss the narrower conclusions of this specific task, and close with more general discussion of the RFI problem in microwave radiometry and what this project may have elucidated for the NWP community going forward.

The flags from EORFIScan largely confirmed expectations of RFI from the literature, namely that affected frequencies are roughly 19 GHz and below, with more prevalent and intense sources at the lowest frequencies (C-band). Most of the locations of flagged RFI are reminiscent of Draper (2018) and other studies from several years ago. This is reassuring in a way, as no widespread interference that was previously unknown was discovered here. The caveat is that the dates examined are from two years ago (2022) and the RF environment is constantly changing, but there does not yet appear to be a wholesale deterioration of the efficacy of these bands due to interference.

Departure-based analysis found that the main features of interference identified by EORFIScan were corroborated with systematic, positive departures. At the lower frequency bands of AMSR2, most of the main features were found to have consistently positive departures in the IFS, indicative of likely RFI whether over sea or land. To make these assessments, the radiances analysed were limited to locations where the model background simulations are well-trusted. These screening choices largely followed those of microwave imager assimilation in the IFS, avoiding cold surfaces, high orography, and so on. A deliberate decision was made not to screen out clouds or precipitation for the analysis. The study's working assumption was that all-sky simulations (i.e. including cloud and precipitation) were adequate for analysing RFI signals, with the understanding that (1) the most pernicious forward model biases are removed by the aforementioned screening based on scene type and (2) all-sky displacement errors are largely symmetrical. It is an open question if this is a fair assumption particularly at C-band and X-band channels that have received less attention in NWP and forward model development.

The performance of EORFIScan was notably disparate for the different frequency bands studied. It

appeared most skilful at C-band channels, where atmospheric sensitivity is lowest and the strongest hydrometeor impacts on TB are typically less than maximal RFI signals. For 10.65 GHz over sea, the flagging was more cautious, possibly balancing atmospheric sensitivity and conservative coastal screening against false positives. At 18.7 GHz very little RFI was detected other than around the USA, though some clear weather-related signals (i.e. false positives) start to be more common at this more precipitation-sensitive frequency. At 23 GHz and higher frequencies, the flagged points were generally attributable to this type of false positive, with sea-ice edges, coastlines, and precipitation features identified as potential causes, though it is hard to be certain that no RFI exists in isolated instances at these bands. A few persistent features appeared across several channels, such as likely false positives near Baja California or east of the Arabian Peninsula; it is not clear what may have caused these, but some combination of ocean upwelling and dry, possibly dusty atmospheric conditions may have contributed. Overall the prevalence of false positives was quite low, as judged by the fraction of near-zero and negative departures flagged as RFI—small fractions of a percent for most bands.

Because there is no definitive truth for RFI-affected observations, it is difficult to say anything quantitative about detection limits, missed RFI, and false alarm ratios here. For instance, in the case of 10.65 GHz interference in the seas around Europe, the departure analysis shows that EORFIScan identifies many observations with a roughly +10 K departure that do appear to be RFI and can be linked to known sources. On the other hand, there are instances of probable RFI identified in the departures that were not flagged, such as near coastlines. However, this does not tell us the detection limit for this band or give a sense of the fraction of likely RFI instances identified. Particularly over sea it would be feasible to analyse these cases further by using other aspects of the model background (e.g. precipitation, high winds) to effectively narrow the PDF of departures and make RFI more apparent, but that was not done here.

Along the same lines, the difference in detection for V- vs. H-pol channels (see Fig. 15) may signal a limitation of the model-agnostic approach of EORFIScan. In principle, RFI should exhibit similar magnitudes at either polarisation—a 20 K RFI signal should manifest similarly despite the radiative temperature of the background. Although the ocean is radiatively colder at H-pol due to an emissivity roughly half that of V-pol, the signal from potential interference should not be larger at H-pol, though of course sources that emit at one polarisation or the other will manifest uniquely. However, geophysical signals such as clouds, precipitation, and ocean roughness are all ways to increase H-pol TB roughly twice as much as at V-pol. The hypothesis is thus that EORFIScan is more cautious in ascribing RFI at H-pol channels, using thresholds that are perhaps twice those of V-pol channels (though 10.65 GHz over sea is an intriguing exception).

Although not explored here, it may be fruitful to consider departure-based flagging in the future, especially for the low-level RFI that is so pernicious at low frequencies over ocean. Direct comparison of departures at nearby frequency bands may be a useful tool for RFI identification in addition to model-independent approaches, and V- vs. H-pol differences could also be examined in this context. And whether departure-based or model-independent, in consideration of the ever-changing RF environment, it would be a real step forward to have RFI monitoring systems available close to real time so that mitigation efforts can be more responsive to emerging threats.

In the larger context of RFI and microwave radiometry in data assimilation, it is clear that the increased exploitation of radiances from low-frequency bands in coupled Earth Systems will need to address the wide-spread RFI present. An example of such increased exploitation is the use of ocean-surface temperature information from frequencies in the 6-10 GHz range currently under development at ECMWF, and this places strong demands on the quality of the surface-temperature signals. Flags such as those evaluated here could be helpful in this regard, though better performance near coastlines and a low detection

limit would probably be needed. In contrast, higher frequency bands are better understood by NWP systems as many of these channels have been assimilated for years, but little to no interference was found or corroborated at the more cloud-sensitive frequencies at the time of this study, March and October 2022. This is a positive finding, but vigilance will be needed particularly in the V-band of oxygen channels, as low-level RFI there could be very detrimental to forecast skill.

Appendix

This appendix contains figures complementary to those in the main text. These include figures showing October rather than March 2022, H-pol rather than V-pol, a view of superobbed (rather than native resolution) radiances, and a plot of land rather than ocean data.
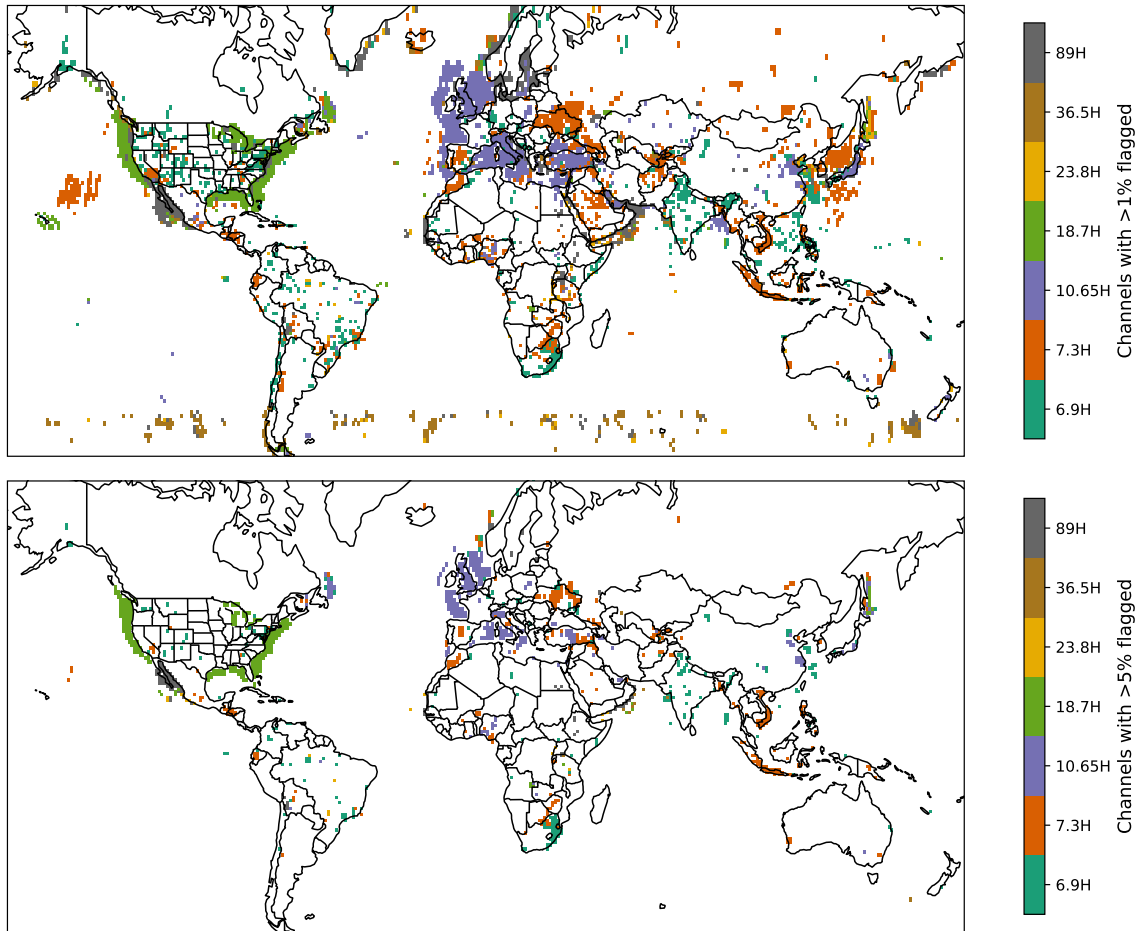

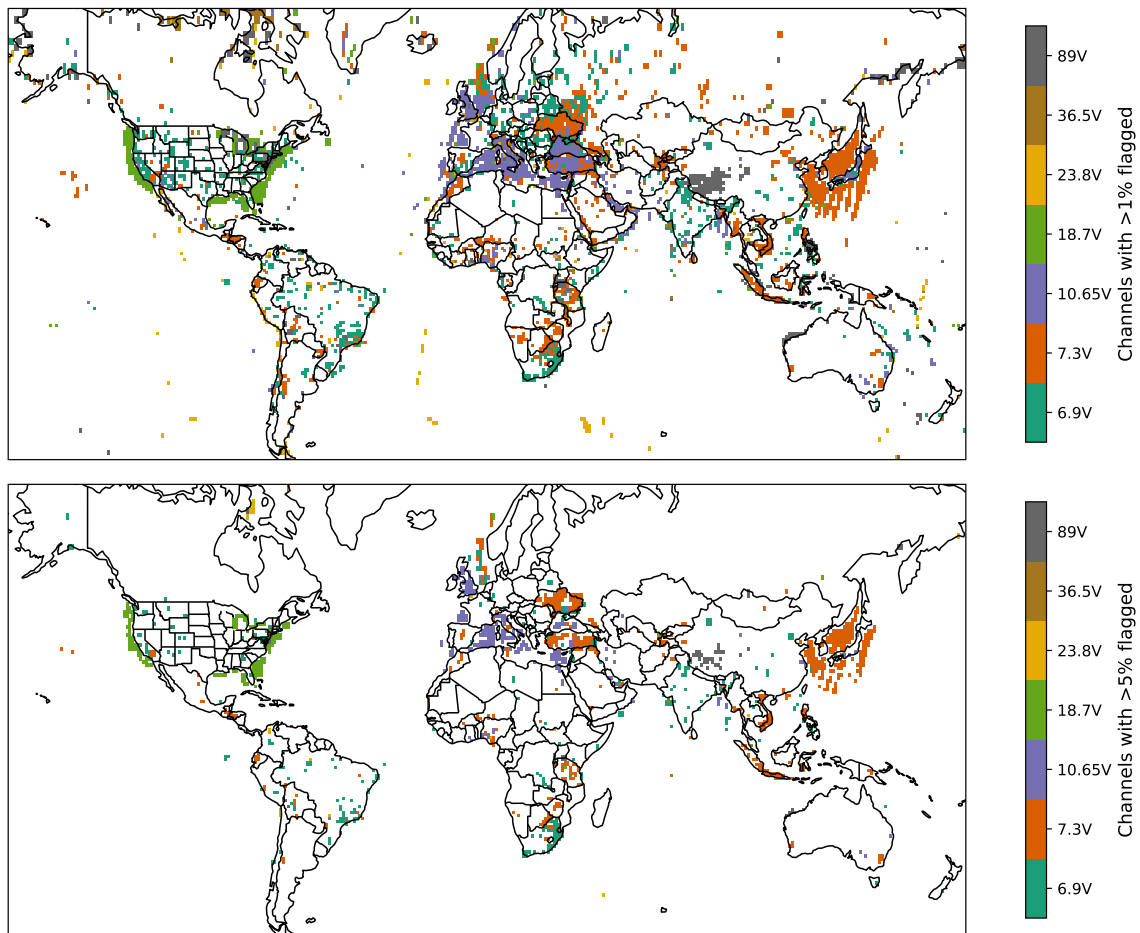*Figure 22: As Fig. 5 but for H-pol channels, March 2022.*

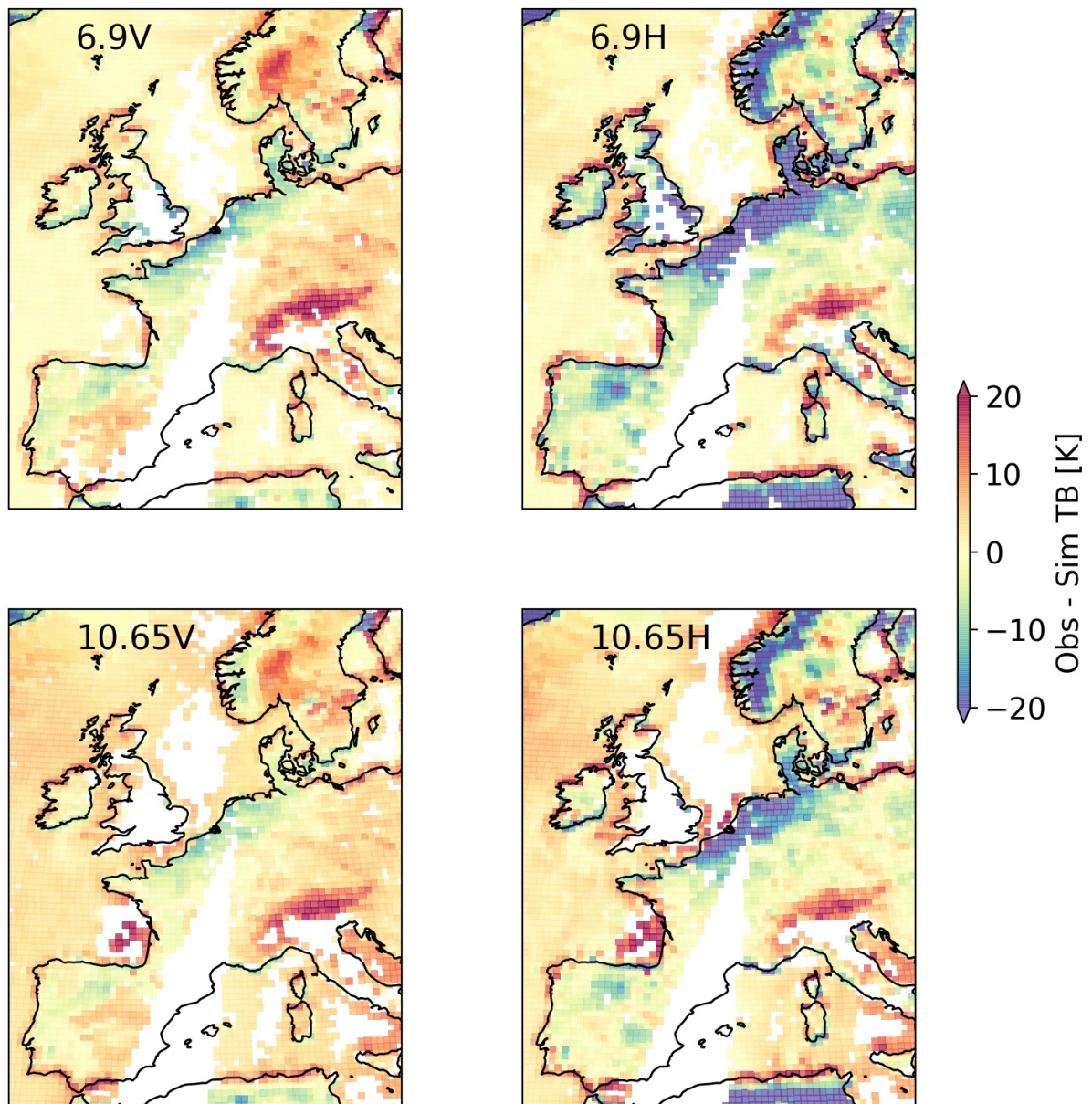*Figure 23: As Fig. 5 but for October 2022.*

Figure 24: From a special experiment with bit-wise averaging applied to all radiances that exist within a 40 km box, here we show superobbed AMSR2 radiances for the same date as Figs. 7 and 10. Any superob that contains one or more constituent radiances with an RFI flag set is removed, i.e. this is a map of superobbed radiances with all RFI from EORFIScan screened out but with no other IFS screening. Note that the projection is slightly different to permit showing the superob boxes on an equal-area grid as squares.
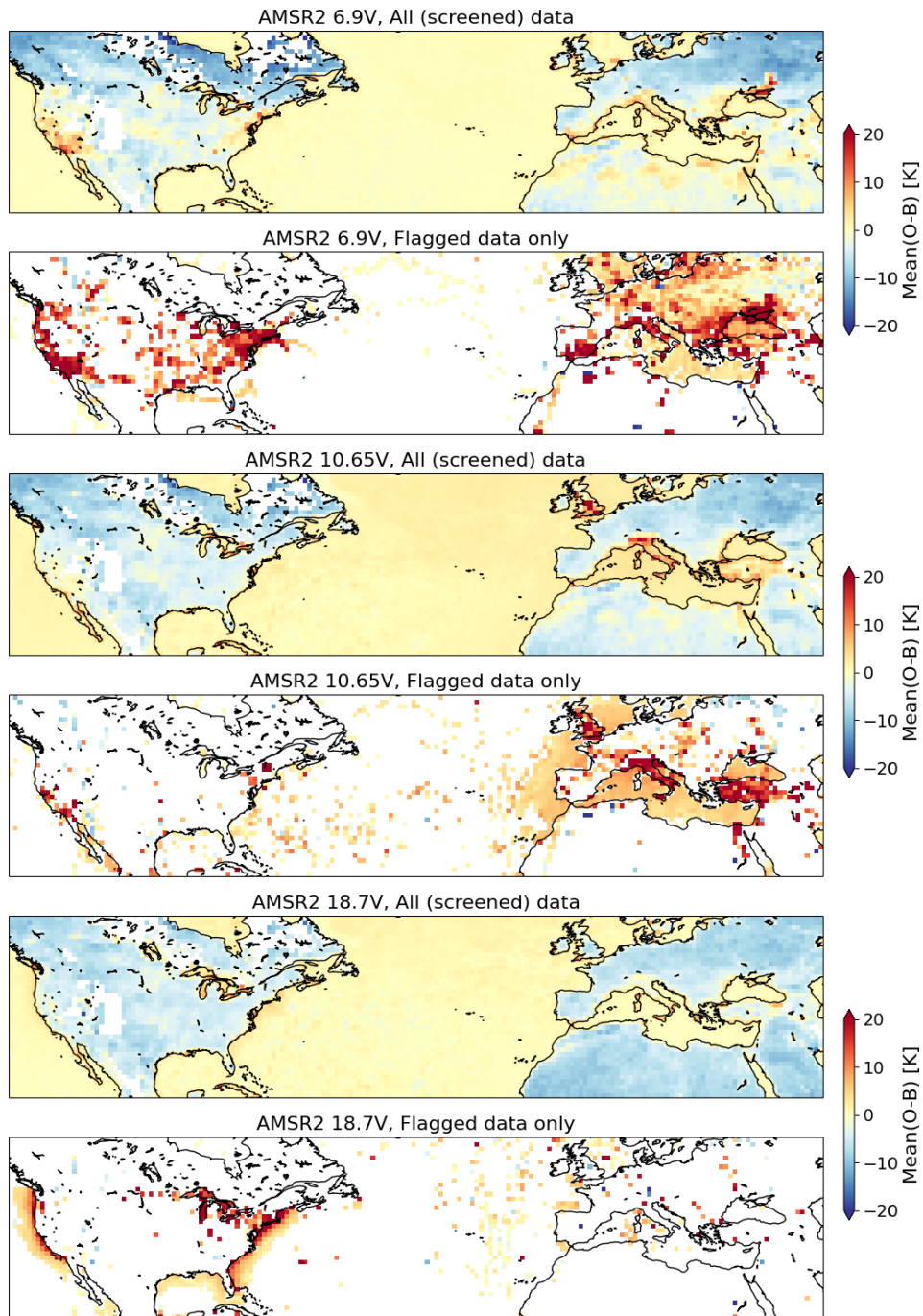
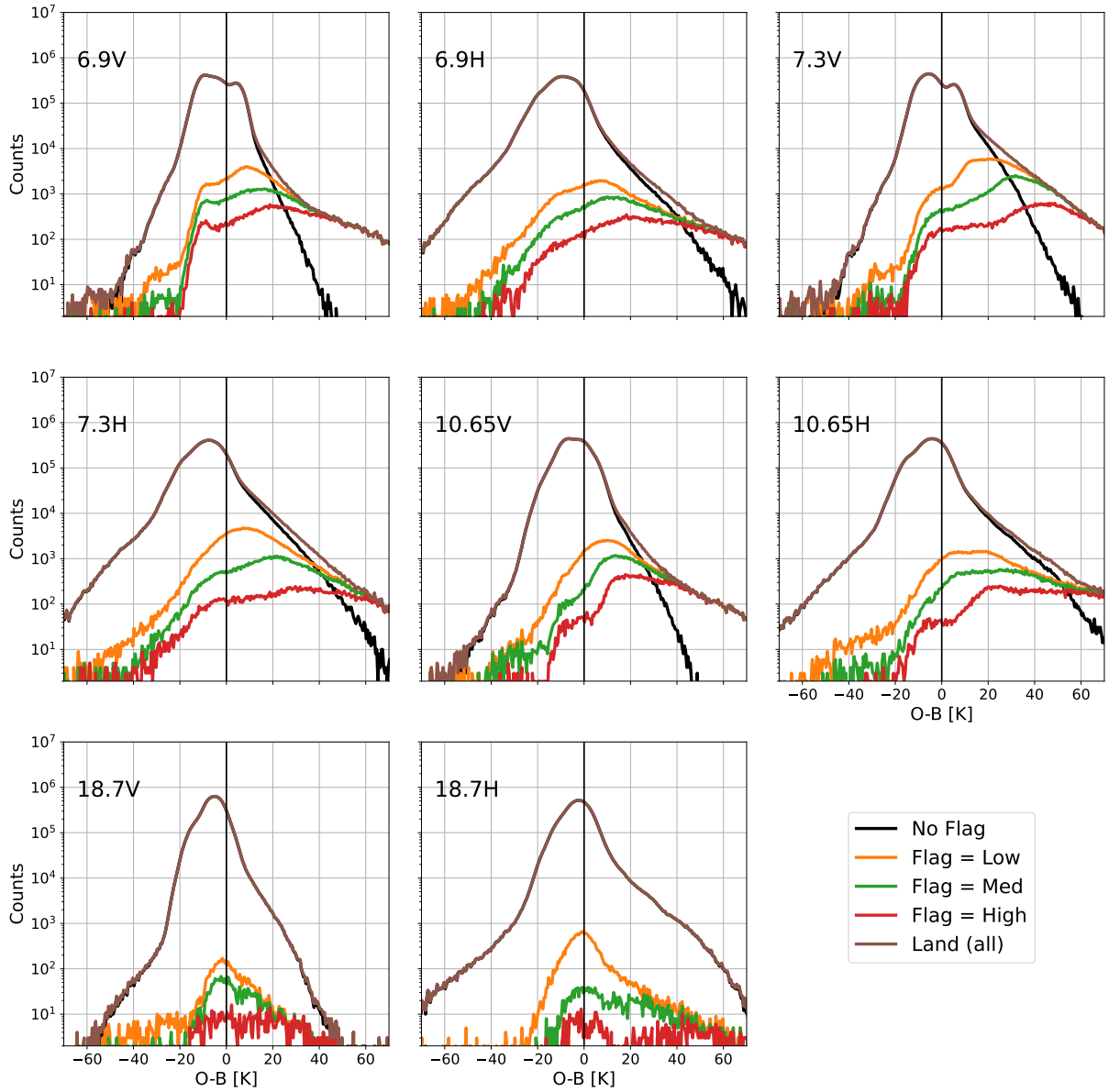*Figure 25: As Fig. 11 but covering October.*

Figure 26: Histograms of departures for screened observations over land. The region covers North America and Europe, for the month of October 2022. Compare to the figure covering data over sea in Fig. 18.

Acknowledgements

Glossary

AMSR-E Advanced Microwave Scanning Radiometer for EOS. 3

AMSR2 Advanced Microwave Scanning Radiometer-2. 6

AMSR3 Advanced Microwave Scanning Radiometer-3. 6

AMSU-A Advanced Microwave Sounding Unit-A. 6

ATMS Advanced Technology Microwave Sounder. 7

BUFR Binary Universal Format for the Representation of meteorological data. 13

CAO Cold air outbreak. 18

CIMR Copernicus Imaging Microwave Radiometer. 6

ECT Equator crossing time. 6

EESS Earth Exploration-Satellite Service. 2

EORFIScan Earth Observation RFI Scan software. 9

FOV Field of view (instantaneous). 7

GCOM-W Global Change Observation Mission-Water. 6

GPM Global Precipitation Measurement. 5

GRDS Ground RFI Detection System. 9

IFS Integrated Forecasting System. 12

ITU International Telecommunications Union. 2

MWS MicroWave Sounder. 7

RDA Research and Development in Aerospace. 9

RFI Radio Frequency Interference. 2

RTTOV-SCATT Radiative transfer for TOVS microwave scattering package. 14

SFCG Space Frequency Coordination Group. 2

SMAP Soil Moisture Active-Passive. 3

SMOS Soil Moisture and Ocean Salinity. 3

SPCZ South Pacific Convergence Zone. 9

SRF Spectral response function. 2

SST Sea surface temperature. 6

SURFEM-Ocean Surface Fast Emissivity Model for Ocean. 14

TB Brightness temperature. 13

TMI Tropical Rainfall Measuring Mission (TRMM) Microwave Imager. 4

WRC World Radiocommunication Conference. 2

ZBT Zenithal Blue Technologies. 9

References

Adams, I. S., Bettenhausen, M. H., Gaiser, P. W. and Johnston, W. (2010). Identification of ocean-reflected radio-frequency interference using WindSat retrieval chi-square probability. *IEEE Geosci. Remote Sens. Lett.*, **7**(2), 406–410, doi:10.1109/LGRS.2009.2037446, URL https://ieeexplore.ieee.org/document/5398988.

Baordo, F. and Geer, A. J. (2016). Assimilation of SSMIS humidity-sounding channels in all-sky conditions over land using a dynamic emissivity retrieval. *Quart. J. Roy. Meteor. Soc.*, **142**(700), 2854–2866, doi:10.1002/qj.2873, URL https://rmets.onlinelibrary.wiley.com/doi/abs/10.1002/qj.2873.

Berg, W., Bilanow, S., Chen, R., Datta, S., Draper, D., Ebrahimi, H., Farrar, S., Jones, W. L., Kroodsma, R., McKague, D., Payne, V., Wang, J., Wilheit, T. and Yang, J. X. (2016). Intercalibration of the GPM microwave radiometer constellation. *J. Atmos. Oceanic Technol.*, **33**(12), 2639–2654, doi:10.1175/JTECH-D-16-0100.1, URL https://journals.ametsoc.org/view/journals/atot/33/12/jtech-d-16-0100_1.xml.

Bormann, N. (2017). Slant path radiative transfer for the assimilation of sounder radiances. *Tellus A*, **69**(1), 1272779, doi:10.1080/16000870.2016.1272779, URL https://doi.org/10.1080/16000870.2016.1272779.

Dee, D. P. (2004). Variational bias correction of radiance data in the ECMWF system. In *ECMWF workshop proceedings: Assimilation of high spectral resolution sounders in NWP, 28 June – 1 July, 2004*, pp. 97–112, ECMWF, Reading, UK, URL https://www.ecmwf.int/sites/default/files/elibrary/2004/74143-variational-bias-correction-radiance-data-ecmwf-system_0.pdf.

Draper, D. (2015). Report on GMI special study 15: radio frequency interference. *Technical report*, NASA Contractor Report, URL https://ntrs.nasa.gov/api/citations/20160003316/downloads/20160003316.pdf.

Draper, D. W. (2017). Terrestrial and space-based RFI observed by the GPM microwave imager (GMI) within NTIA semi-protected passive earth exploration bands at 10.65 and 18.7 GHz. In *Proceedings of 2016 Radio Frequency Interference: Coexisting with Radio Frequency Interference, RFI 2016*, ISBN 9781509062010, doi:10.1109/RFINT.2016.7833526, URL https://ieeexplore.ieee.org/document/7833526.

Draper, D. W. (2018). Radio frequency environment for earth-observing passive microwave imagers. *IEEE J. Sel. Top. Appl. Rem. Sens.*, **11**(6), 1–10, doi:10.1109/JSTARS.2018.2801019, URL https://ieeexplore.ieee.org/document/8315049.

Draper, D. W. and Newell, D. A. (2015). An assessment of radio frequency interference using the GPM microwave imager. In *2015 IEEE International Geoscience and Remote Sens. Symposium, IGARSS 2015, Milan, Italy, July 26-31, 2015*, pp. 5170–5173, doi:10.1109/IGARSS.2015.7326998, URL https://ieeexplore.ieee.org/document/7326998.

Draper, D. W., Newell, D. A., Wentz, F. J., Krimchansky, S. and Skofronick-Jackson, G. M. (2015). The Global Precipitation Measurement (GPM) microwave imager (GMI): Instrument overview and early on-orbit performance. *IEEE J. Sel. Top. Appl. Rem. Sens.*, **8**(7), 3452–3462, doi:10.1109/JSTARS.2015.2403303, URL https://ieeexplore.ieee.org/document/7052302.

Draper, D. W. and Stocker, E. F. (2017). A comparison of radio frequency interference within and outside of allocated passive earth exploration bands at 10.65 GHz and 18.7 GHz using the GPM Microwave Imager and WindSat. In *2017 IEEE International Geoscience and Remote Sensing Symposium (IGARSS)*, pp. 2731–2733, doi:10.1109/IGARSS.2017.8127561, URL https://ieeexplore.ieee.org/document/8127561.

Duncan, D. I., Bormann, N. and Geer, A. J. (2022a). All-sky assimilation of AMSU-A window channels. *Technical Report 59*, EUMETSAT/ECMWF Fellowship Programme Research Report, Shinfield Park, Reading, doi:10.21957/daefm16p8, URL https://www.ecmwf.int/node/20457.

Duncan, D. I., Bormann, N., Geer, A. J. and Weston, P. (2022b). Assimilation of AMSU-A in all-sky conditions. *Mon. Weather Rev.*, **150**(5), 1023 – 1041, doi:10.1175/MWR-D-21-0273.1, URL https://doi.org/10.1175/MWR-D-21-0273.1.

Duncan, D. I., Geer, A., Bormann, N. and Dahoui, M. (2024). Vicarious calibration monitoring of MWI and ICI using NWP fields. *Technical report*, EUMETSAT Contract Report, doi:10.21957/7c2d18d2e1, URL https://www.ecmwf.int/en/elibrary/81563-vicarious-calibration-monitoring-mwi-and-ici-using-nwp-fields.

ECMWF (2023). *IFS Documentation CY48R1 - Part II: Data Assimilation*, chapter 2, p. 108. 2, ECMWF, doi:10.21957/a744f32e74, URL https://www.ecmwf.int/en/elibrary/81368-ifs-documentation-cy48r1-part-ii-data-assimilation.

English, S., Duncan, D. and Turner, E. (2020). Assessment of value of provision of spectral response functions from CGMS agencies. In *CGMS-48 WG II*, URL https://www.researchgate.net/publication/351358361_Assessment_of_Value_of_Provision_of_Spectral_Response_Functions_from_CGMS_Agencies.

Geer, A. J. (2024). Joint estimation of sea ice and atmospheric state from microwave imagers in operational weather forecasting. *preprint*, doi:10.22541/essoar.170431213.35796940/v1, URL http://dx.doi.org/10.22541/essoar.170431213.35796940/v1.

Geer, A. J., Bauer, P., Lonitz, K., Barlakas, V., Eriksson, P., Mendrok, J., Doherty, A., Hocking, J. and Chambon, P. (2021). Bulk hydrometeor optical properties for microwave and sub-millimetre radiative transfer in RTTOV-SCATT v13.0. *Geosci. Model Dev.*, **14**(12), 7497–7526, doi:10.5194/gmd-14-7497-2021, URL https://gmd.copernicus.org/articles/14/7497/2021/.

Geer, A. J., Lonitz, K., Duncan, D. I. and Bormann, N. (2022). Improved surface treatment for all-sky microwave observations. *Technical Report 894*, ECMWF Tech. Memo., Shinfield Park, Reading, doi:10.21957/zi7q6hau, URL https://www.ecmwf.int/node/20337.

Group, S. F. C. (2022). Analysis of worst case RFI levels affecting EESS (passive) sensors from 1.4 to 252 GHz. *Technical Report SFCG 41-3*, SFCG, URL https://www.sfcgonline.org/Reports/REP%20SFCG%2041-3%20(Max%20RFI%20in%20EESS-passive%20bands).pdf.

Karbou, F., Gérard, E. and Rabier, F. (2006). Microwave land emissivity and skin temperature for AMSU-A and -B assimilation over land. *Quart. J. Roy. Meteor. Soc.*, **132**(620), 2333–2355, doi:10.1256/qj.05.216, URL https://rmets.onlinelibrary.wiley.com/doi/abs/10.1256/qj.05.216.

Kilic, L., Prigent, C., Jimenez, C., Turner, E., Hocking, J., English, S., Meissner, T. and Dinnat, E. (2023). Development of the SURface Fast Emissivity Model for Ocean (SURFEM-Ocean)

based on the PARMIO radiative transfer model. *Earth Space Sci.*, **10**(11), e2022EA002785, doi:10.1029/2022EA002785, URL https://agupubs.onlinelibrary.wiley.com/doi/abs/10.1029/2022EA002785.

Le Vine, D. M. (2019). RFI and remote sensing of the earth from space. *Journal of Astronomical Instrumentation*, **08**(01), 1940001, doi:10.1142/S2251171719400014, URL https://doi.org/10.1142/S2251171719400014.

Li, L., Njoku, E. G., Im, E., Chang, P. S. and Germain, K. S. (2004). A preliminary survey of radio-frequency interference over the U.S. in Aqua AMSR-E data. *IEEE T. Geosci. Remote Sens.*, doi:10.1109/TGRS.2003.817195, URL https://ieeexplore.ieee.org/document/1266727.

Lonitz, K. and Geer, A. J. (2015). New screening of cold-air outbreak regions used in 4D-Var all-sky assimilation. *Technical Report 35*, EUMETSAT/ECMWF Fellowship Programme Research Report, Shinfield Park, Reading, URL https://www.ecmwf.int/node/10777.

Maeda, T., Taniguchi, Y. and Imaoka, K. (2016). GCOM-W1 AMSR2 level 1R product: Dataset of brightness temperature modified using the antenna pattern matching technique. *IEEE T. Geosci. Remote Sens.*, **54**(2), 770–782, doi:10.1109/TGRS.2015.2465170, URL https://ieeexplore.ieee.org/document/7244183.

McKague, D., Puckett, J. J. and Ruf, C. (2010). Characterization of K-band radio frequency interference from AMSR-E, WindSat and SSM/I. In *2010 IEEE International Geoscience and Remote Sensing Symposium*, pp. 2492–2494, doi:10.1109/IGARSS.2010.5651860, URL https://ieeexplore.ieee.org/document/5651860.

Njoku, E., Ashcroft, P., Chan, T. and Li, L. (2005). Global survey and statistics of radio-frequency interference in AMSR-E land observations. *IEEE Trans. Geosci. Remote Sens.*, **43**(5), 938–947, doi:10.1109/TGRS.2004.837507, URL https://ieeexplore.ieee.org/document/1424270.

Okuyama, A. and Imaoka, K. (2015). Intercalibration of Advanced Microwave Scanning Radiometer-2 (AMSR2) brightness temperature. *IEEE Trans. Geosci. Remote Sens.*, **53**(8), 4568–4577, doi:10.1109/TGRS.2015.2402204, URL https://ieeexplore.ieee.org/document/7057660.

Oliva, R., Daganzo, E., Richaume, P., Kerr, Y., Cabot, F., Soldo, Y., Anterrieu, E., Reul, N., Gutierrez, A., Barbosa, J. and Lopes, G. (2016). Status of radio frequency interference (RFI) in the 1400–1427MHz passive band based on six years of SMOS mission. *Rem. Sens. Environment*, **180**, 64–75, doi:https://doi.org/10.1016/j.rse.2016.01.013, URL https://www.sciencedirect.com/science/article/pii/S0034425716300141, special Issue: ESA's Soil Moisture and Ocean Salinity Mission - Achievements and Applications.

Oliva, R., Onrubia, R., Martellucci, A., Daganzo-Eusebio, E., Jorge, F., Soldo, Y., English, S., De Rosnay, P., Weston, P., Barbosa, J. and Nestoras, I. (2021). Results from the ground RFI detection system for passive microwave earth observation data. In *2021 IEEE International Geoscience and Remote Sensing Symposium IGARSS*, pp. 1827–1830, doi:10.1109/IGARSS47720.2021.9553636, URL https://ieeexplore.ieee.org/document/9553636.

Palmer, R., Whelan, D., Bodine, D., Kirstetter, P., Kumjian, M., Metcalf, J., Yeary, M., Yu, T.-Y., Rao, R., Cho, J., Draper, D., Durden, S., English, S., Kollias, P., Kosiba, K., Wada, M., Wurman, J., Blackwell, W., Bluestein, H., Collis, S., Gerth, J., Tuttle, A., Wang, X. and Zrnić, D. (2021). The need for spectrum and the impact on weather observations. *Bulletin of the American Meteorological Society*, **102**(7), E1402 – E1407, doi:10.1175/BAMS-D-21-0009.1, URL https://journals.ametsoc.org/view/journals/bams/102/7/BAMS-D-21-0009.1.xml.

Robel, J. and Graumann, A. (2014). NOAA KLM user's guide with NOAA-N, N Prime, and MetOp supplements. *Technical report*, NOAA NESDIS, URL https://lccn.loc.gov/2009578433.

Scanlon, T., Geer, A., Bormann, N. and Browne, P. (2024). Improving ocean surface temperature for NWP using all-sky microwave imager observations. *Technical Report 64*, EUMETSAT/ECMWF Fellowship Programme Research Report, Shinfield Park, Reading, doi:10.21957/c16be07b23, URL https://www.ecmwf.int/en/elibrary/81580-improving-ocean-surface-temperature-nwp-using-all-sky-microwave-imager.

Wentz, F. J. (2015). A 17-yr climate record of environmental parameters derived from the Tropical Rainfall Measuring Mission (TRMM) Microwave Imager. *J. Climate*, **28**(17), 6882 – 6902, doi: 10.1175/JCLI-D-15-0155.1, URL https://journals.ametsoc.org/view/journals/clim/28/17/jcli-d-15-0155.1.xml.

Wentz, F. J. and Draper, D. (2016). On-orbit absolute calibration of the Global Precipitation Measurement Microwave Imager. *J. Atmos. Oceanic Technol.*, doi:10.1175/JTECH-D-15-0212.1, URL https://journals.ametsoc.org/view/journals/atot/33/7/jtech-d-15-0212_1.xml.

Weston, P., de Rosnay, P. and English, S. (2021). GRDS test-bed report. *Technical report*, ESA Contract Report, doi:10.21957/8kv6wj087, URL https://www.ecmwf.int/en/elibrary/81228-grds-test-bed-report.

Wu, Y., Li, M., Bao, Y. and Petropoulos, G. P. (2020). Cross-validation of radio-frequency-interference signature in satellite microwave radiometer observations over the ocean. *Remote Sens.*, **12**(20), doi: 10.3390/rs12203433, URL https://www.mdpi.com/2072-4292/12/20/3433.

Wu, Y., Qian, B., Bao, Y., Li, M., Petropoulos, G. P., Liu, X. and Li, L. (2019). Detection and analysis of C-band radio frequency interference in AMSR2 data over land. *Remote Sens.*, **11**(10), doi:10.3390/rs11101228, URL https://www.mdpi.com/2072-4292/11/10/1228.

Zabolotskikh, E. V., Mitnik, L. M. and Chapron, B. (2015). Radio-frequency interference identification over oceans for C- and X-band AMSR2 channels. *IEEE Geosci. Remote Sens. Lett.*, **12**(8), 1705–1709, doi:10.1109/LGRS.2015.2420120, URL https://ieeexplore.ieee.org/document/7095532.

Zou, X., Tian, X. and Weng, F. (2014). Detection of television frequency interference with satellite microwave imager observations over oceans. *J. Atmos. Oceanic Technol.*, **31**(12), 2759 – 2776, doi:10.1175/JTECH-D-14-00086.1, URL https://journals.ametsoc.org/view/journals/atot/31/12/jtech-d-14-00086_1.xml.